Ring-Shaped Silicon Photonic Crystal Structures for Bio-Sensing and Optical-Interconnects

By

Ming Gai Stanley Lo

Dissertation
Submitted to the Faculty of the
Graduate School of Vanderbilt University
in partial fulfillment of the requirements
for the degree of

DOCTOR OF PHILOSOPHY
in
Electrical Engineering

March 31, 2018
Nashville, TN

Approved:
Philippe Fauchet, Ph.D., Chair
Ronald Schrimpf, Ph.D.
Jason Valentine, Ph.D.
Sharon Weiss, Ph.D.
Yaqiong Xu, Ph.D.

ACKNOWLEDGEMENTS

First and foremost, I would like to thank my Ph.D. advisor and mentor Philippe Fauchet. For his numerous support and guidance, both in academic research and life, during the last couple of years of my PhD study. I still remember the moment when I desired to study aboard for becoming a better researcher to contribute the field, Prof. Fauchet provided me a valuable opportunity to work in his research group for interesting projects in silicon photonics and nano-photonics. I truly believe all the research techniques and problem solving skills I learned in last couple years will be beneficial for me during my career, as an engineer and as a researcher. Thank you so much for everything, Philippe.

I would also like to express my appreciation to the other committee members who made a lot of helpful comments during the whole process of refining my research directions. Thank you Prof. Ronald Schrimpf, Prof. Jason Valentine and Prof. Sharon Weiss and Prof. Yaqiong Xu.

I also wish to thank the researchers and collaborators I had work with, both in Vanderbilt and University of Rochester. Thank you for Prof. Weiss and her research group members Shuren Hu, Girija Gaur for collaboration in the biosensing project. I also need to thank Sharon for all her mentoring and guidance in last few years in Vanderbilt. Thanks Prof. Yiorgos Kostoulas for the time we work together for the novel nano-beam structures. Thanks Prof. Xu for some of early discussions on PhCR projects. I would also like to thank Prof. Qiang Lin and Dr. Jonathan Lee from University of Rochester for providing me the opportunities to work in the lab for experiments used in PhCR projects.

My heartfelt thanks also go to all the Fauchet group members, Halina Krzyzanowska, Maryna Kalavanka, Jonathan Lee, Krishanu Shome, Adam Heiniger, Josh Winans, Karl Ni, Joe Qi and Chanse Hungerford. Especially Joe and Chanse, since it is always not easy to start a new lab, I am glad that I can had you guys to work together when the group moved to Vanderbilt.

My special thanks go to the cleanroom staff in the CNMS, Oak Ridge National Lab. Thank you Scott, Dayrl, Dale, Kevin, Ivan and Bandatae. I would also like to thank Devin Brown from GATECH for his kind help during all of my visits for using the EBL system onsite.

Finally, I would like to thank my family, my friends for all their supports. During my difficult times, their conditional supports and love always guide me back to strive my goal for success.

TABLE OF CONTENTS

LIST OF TABLES

LIST OF FIGURES

1. Introduction

In this chapter, the background of research fields related to the ring-shaped silicon photonic crystal devices are introduced. As the ring-shaped photonic crystal devices are integrated optical devices belong to the big family of photonic integrated circuits, we will first the field of photonic integrated circuit (PIC) and what are its similarities/differences compared to microelectronics. Second, as the ring-shaped photonic crystal devices used silicon as the optical material, the overall historical background of silicon photonics will be presented. In that section, the advantages and challenges of silicon photonics compared to other material platform will also be discussed. Finally, the background of optical resonators and photonic crystals will be introduced, as ring-shaped silicon photonic crystal devices are special type of optical resonators by employing photonic crystal structures. At the end of this chapter, thesis objectives and outline will be presented.

1.1 Photonic integrated circuits

Photonic integrated circuits (PIC) are devices that integrate multiple photonic functions by integrating different optical device elements in a same planar platform, which is analogous to an electronic integrated circuit (IC) in microelectronic industry. The major difference between a PIC and an electronic IC is that a PIC provides functionality on optical signals rather than electrical signals in an electronic IC. Also, PIC integrates various discrete optical devices such as the lasers, amplifiers, photodetectors, optical

modulators, optical filters etc., while electronic IC primary integrates millions to billions of transistors in a single tiny chip. Table 1.1 shows the overview of technology comparison between photonic (including PIC) and microelectronic industry.

	Photonic components	Electronic IC
Repeatable building blocks	None (laser, photodetector, modulator, filter, etc.)	Transistors
Dominant material platforms	None (InP, GaAs, polymer, Si, etc.)	Silicon
Dominant manufacturing processes	None (Hybrid, monolithic, active, passive, etc.)	CMOS

Table 1.1. Comparison between photonic industry and microelectronic industry of building blocks, material platforms and manufacturing processes.

In the current photonic industry, a variety of materials have been employed in each commercial discrete device. For example, the indium phosphide (InP) material has been use as a substrate for the lasers emitting in 1550 nm (C-band), lithium niobate ($LiNbO_3$) has been employed for making optical modulators, silica used for optical fiber, silica-on-silicon used for passive devices etc. Table 1.2 shows the summary on materials of different discrete photonic devices. From table 1.2, most of the materials used in commercial discrete photonic devices are not compatible to achieve other functionalities. For example, lithium niobate is superb for making optical modulators, however, it is not capable for using as the laser materials. On the other hand, even the III-V semiconductors fulfill all the required functions, the fabrication processes of making different components are different, and it results in big challenges of integration. Due to these limitations, the development of PIC over the last 20-30 years was relatively slow

compare with electronic IC industry. So it is commonly accepted that the development and implementation of photonics will be strongly enhanced if the industrial model of electronic IC can be applied to PIC [1], as microelectronic industry already has a dominant material platform and standardized fabrication process.

	Lasers	Detectors	Modulators	Amplifiers	Passive devices
III-V semiconductors	Dominant	Dominant	Available	Dominant	Available
Lithium niobate			Dominant		Available
Polymers			Available		Available
Silica-on-silicon					Available
Erbium-doped materials	Available			Dominant	Available

Table 1.2. Summary of material platforms used by various discrete photonic components

Figure 1.1 shows the schematics of a PIC on a polymer platform by hybrid integration [2]. This tunable optical transmitter contains at least seven different materials for different functions include the laser, an external tunable cavity, an isolator and a modulator.

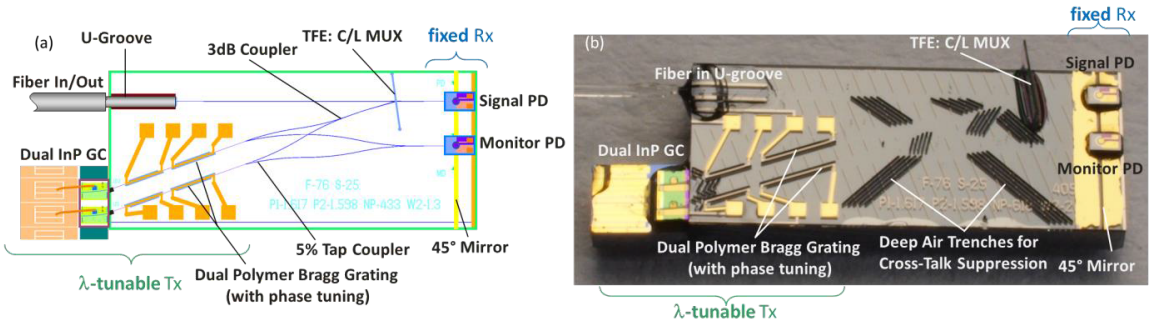

Fig. 1.1. Optical network unit assembled on the polymer-based hybrid integration platform. (a) The schematic layout and (b) photograph of the assembly [2].

This polymer-based PIC was fabricated by a hybrid fabrication process. Although it provided a lower fabrication cost and better functionality than discrete components, a PIC fabricated by monolithic process would still be required to provide even better system functionality and lower cost.

In the early 2000s some convergence appeared to use InP as the substrate material for monolithic PIC. Figure 1.2 shows the historical trend and timeline for monolithic, photonic integration on InP [3]. The development of PIC on InP substrate started in 1980s, with the integration of electronic devices with laser diodes and photodetectors as so-called optoelectronic ICs (OEICs).

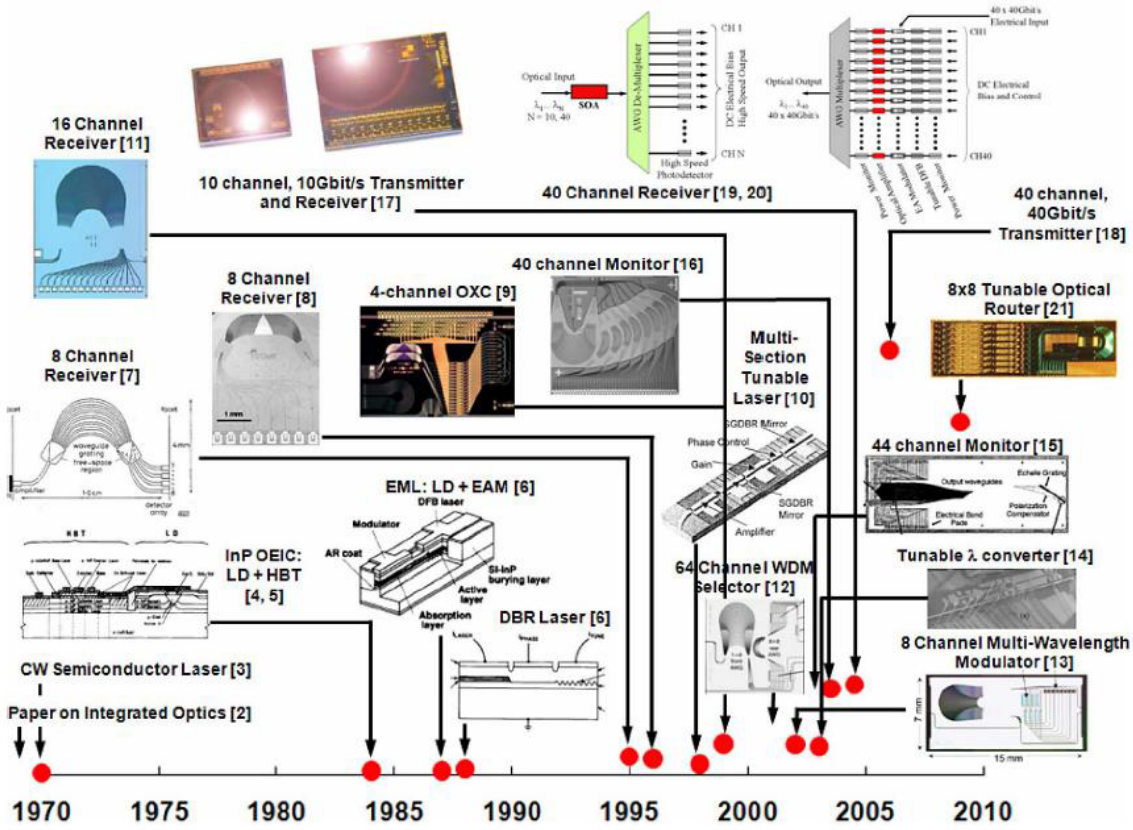

Fig. 1.2. Historical trend and timeline for monolithic, photonic integration on InP [3]. The vertical axis represents the number of photonic components to be integrated.

In late 1980s, the three-section tunable distributed Bragg reflector (DBR) laser was introduced. A while later, the electroabsorption modulator (EAM) integrated to a distributed feedback (DFB) laser was also demonstrated. More components started to be integrated into the InP-based PIC including the semiconductor optical amplifier (SOA) and arrayed waveguide grating (AWG). Recently [3], the research team in University of California, Santa Barbara (UCSB) reported an 8 x 8 monolithic tunable router with about 200 components in a single PIC chip. It is no doubt that InP-based PIC platform is an ideal candidate for telecommunications usage in 1.3-1.6 μm wavelength. However, it also has certain limitations that not only limit the development of PICs, but also become a

roadblock of the whole photonic industry.

In the photonic industry, other material platforms such as silica have also been widely used as different photonic functional devices such as AWG for wavelength division multiplexing (WDM) applications. Since 2000 [1], another material platform – silicon-on-insulator (SOI) has attracted lots of attention on its potential as a substrate for PIC because of low cost and high-density integration. The details on PIC developed on SOI and related research field, silicon photonics, will be discussed in next section.

Unlike in electronic IC, where silicon is a dominant material accounting for over 95% of the whole market of semiconductor chips [1], today's PICs use a variety of materials such as silica (on silicon substrates), III-V-based semiconductor materials such as gallium arsenide (GaAs) and indium phosphide (InP), polymers, lithium niobate and SOI. Different materials have their advantages and limitations on the functions to be integrated. For example, the InP platform enables monolithic integration of the lasers, modulators, photodetectors and other passive components. However, the relatively high fabrication cost limits the potential usage of these devices in telecommunications and computer interconnect regime. Table 1.3 lists the comparison among various PIC material platforms.

	Cost	CMOS-compatible	Integration density	Primary Usage
III-V semiconductors	High	No	High	Integrated WDM transceiver
Silica-on-silicon	Low	Yes	Low	Passive devices (e.g. AWG)
Polymers	Low	No	Low	Modulators and hybrid integration platforms
Lithium niobate	Extremely High	No	Low	High speed modulators (for advanced formats)
Silicon-on-insulator	Low	Yes	High	Low-cost optical interconnects

Table 1.3. Comparison among various PIC material platforms.

InP-based PICs dominant today's market in high-end optical communications systems. However, there are suggestions [1, 4-6] that photonics can be further employed in computing systems as interconnects to solve the existing signal latency problems in microelectronic industry. In an overview, the scale of optical interconnects decrease from rack-to-rack, computer-to-computer, board-to-board (inside computer), chip-to-chip and finally on-chip interconnects. As the scale of optical interconnect decreases, the number of required interconnects exponentially increases. Therefore, cost becomes a primary concern in interconnect applications. The secondary concern is the compatibility with existing electronic platform if the on-chip interconnects is finally to be achieved.

For the first concern, InP based PIC does not fulfill as the wafer and fabrication costs are inevitably high. For the second concern, as mentioned above, silicon dominates the microelectronic industry of over 95% of the whole market. Although III-V semiconductors are compatible for electronic device integration in PICs, to integrate with

existing electronic ICs is still a big challenge. To solve these problems and to achieve an eventual success of on-chip interconnects, recent research pay more attention on silicon-based PIC. The related field – silicon photonics, is not only aiming to provide functional devices for communications system, but also the potential as optical interconnects. The history and current research progress of silicon photonics are discussed in next section.

1.2 Silicon photonics

Although the field of integrated optics (the technology used in PIC) has been established in 1969 [7], the proposed use of silicon as a photonic material platform for telecommunications wavelengths in 1.3-1.6 μm (O-band to C-band) only started 16 years later by Soref in 1985 [8-9]. During that time, silicon has already dominated microelectronic industry and silicon based photonics devices like charged-coupled device (CCD) image sensors were commercially available. The reasons of why silicon 'cannot' be the photonic material in telecommunications wavelengths were due to three basic physical limitations:

1) Silicon is an indirect-bandgap semiconductor therefore it lacks of efficient light sources

2) Silicon has a bandgap of 1.12 eV thus it does not detect light in telecommunications wavelengths (1.3-1.6 μm)

3) Silicon is a centro-symmetric crystal so it does not exhibit linear electro-optic (Pockels) effect

For the first material limitation, indirect bandgap of silicon indicates that the radiative recombination of electrons and holes across the bandgap is weak, resulting in extremely low internal quantum efficiency in bulk silicon (10^{-6}). Consequently, silicon lacks of efficient LEDs or electrically pumped lasers. It has been a serious deficiency of using silicon as a PIC platform since, without light sources, a complete suite of photonic components is not available for monolithic on-chip integration.

To discuss the second material limitation, the fact that silicon is transparent above 1.1 μm is like a situation of paradox. Because silicon is transparent in telecommunications wavelengths (1.3-1.6 μm) means that silicon can be used as low-loss optical waveguides, and no material can be transparent to light and detect light at the same time. The major difference of silicon compared with InP platform is that InP-based PIC has capability of bandgap engineering by changing the composition of III-V alloys. Silicon-based platform dose not have this capability therefore it does not provide the functions of wave guiding and light detection on the same material wafer.

For the third material limitation, silicon does not exhibit Pockels effect – a traditional means of achieving modulation of refractive index in a waveguide-based device. The limitation prohibits the usage of silicon as an electro-optical modulator. Although thermal tuning in silicon is available, the speed is limited to 1MHz [5] so it is not suitable for high-speed modulation. Silicon needs another mechanism to achieve refractive index modulation in order to provide functions on high-speed active tuning/modulation.

Because of the above reasons, the research effort in photonic devices on silicon was only modest after the initial work by Soref. There were early work on the passive components, photodetectors by complementary metal-oxide-semiconductor (CMOS) compatible materials and optical modulators by carrier effect in silicon [10].

Besides the deficiency of using silicon as a photonic material in telecommunications wavelengths, silicon has several major advantages that include the mature fabrication technology on silicon by the microelectronic industry (CMOS fabrication process started to dominate in 1990s) and availability of making low-loss passive devices.

Optoelectronic IC (OEIC) to integrate the electronic and photonic components in the

same platform becomes a huge advantage of silicon. As silicon already dominates the microelectronic industry, the development of photonic devices in silicon could enhance both the performance and cost efficiently by the concept of OEIC. Figure 1.3 shows the related concept, a silicon-based OEIC "superchip" proposed by Soref in 1993 [11].

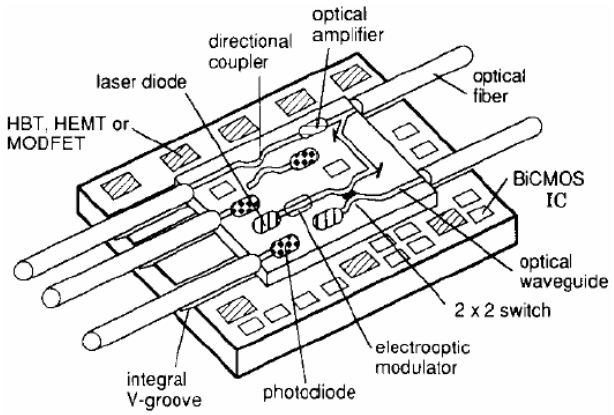

Fig. 1.3. Silicon-based optoelectronic IC "superchip" proposed by Soref in1993 [11]

In year 2000, the manufacturing technologies of high optical quality SOI became mature. A commercially available SOI wafers for photonic usage provide another advantages for silicon photonics – high integration density. This became a catalyst of research in silicon-based photonic devices.

Consequently, the research on photonic devices on silicon increased rapidly after year 2000. The explosion of research efforts led to a stand-alone research field – silicon photonics [12]. The driving force of silicon photonics at that time was mainly by the development of high-volume OEIC and commercial PICs in SOI platform. The field is still very active today and many of the fundamental physical limitations in silicon have been solved by tremendous research efforts over the past 20 years.

For light generation, in order to provide a light source on silicon PIC, integrating the III-V semiconductor lasers to silicon PIC chips by hybrid fabrication method is one of the promising solutions [13]. Although the hybrid method may potentially lead to higher complexity and fabrication costs, the integration of III-V semiconductor lasers to silicon PIC is still a good approach to realize a complete suite of PIC in silicon in current technology limitation.

For light detection, it is feasible for the silicon PIC to detect the light signal in 1.3-1.6 μm by using an integrated germanium (Ge) or silicon-germanium (SiGe) photodetector [14]. Ge and SiGe have advantage of fully compatibility with CMOS process. The state-of-the-art performance of Ge photodetector modules on silicon substrates is already largely compatible with III-V semiconductor-based photodetectors [5] and capable for detecting 40 Gb/s NRZ signals.

For light modulation, as a semiconductor, the refractive index of silicon can be altered by the mean of adding or subtracting its free-carriers. The corresponding effect – free-carrier plasma dispersion effect [10] becomes a major modulation mechanism in silicon for making optical modulators. By optimizing the electrical and photonic structures, one can attain above 40 Gb/s modulation by all silicon based optical modulators [15].

Figure 1.4 shows the overview of Luxtera's silicon PIC that demonstrated in 2005 [16]. The silicon PIC was fabricated by a CMOS-compatible fabrication process. It consists of components of all-silicon modulators, Ge photodetectors, passive photonic devices and electronic circuits. A light source was made by flip-chip bonding techniques of III-V semiconductor lasers emitting in 1.55 μm. This silicon PIC consequently was re-

packaged as active optical cables to provide low-cost optical interconnects in computing centers and data centers.

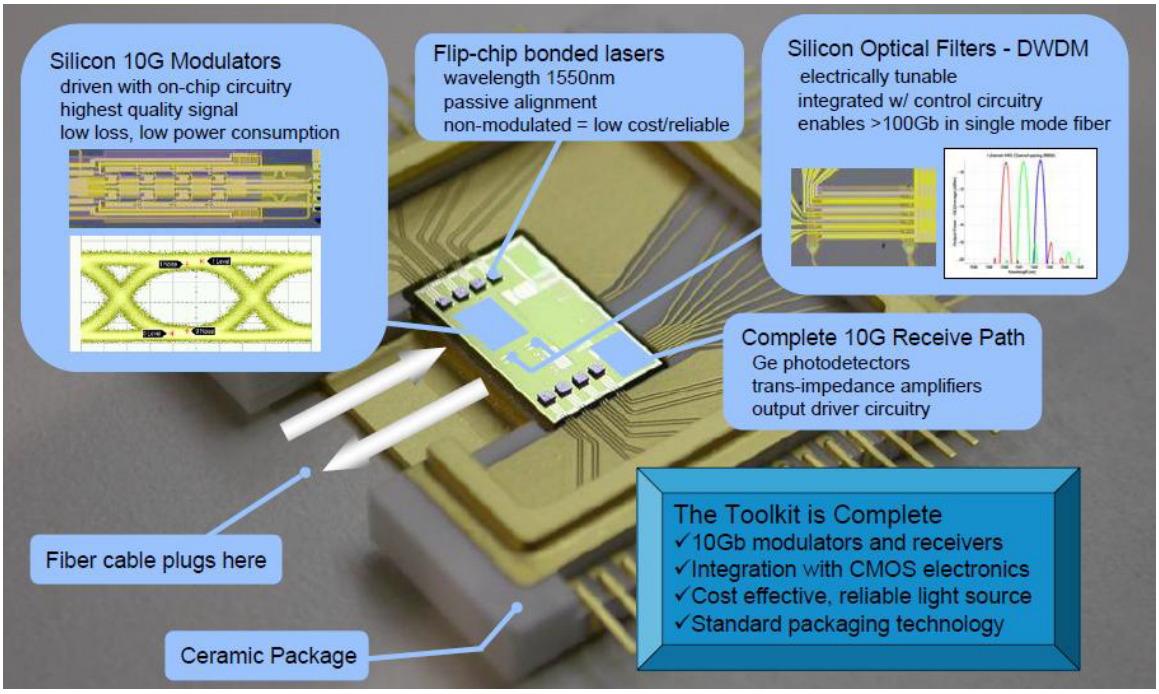

Fig. 1.4. Overview of Luxtera's silicon PIC demonstrated in 2005 [16]

As cost is a big advantage of silicon photonics against III-V semiconductor based photonics, in the followings detailed descriptions of manufacturing cost will be discussed.

The manufacturing costs of PIC can be basically determined by three factors: (a) the cost of substrate per area, (b) the cost of fabrication processes on the substrate per area and (c) the integration densities of the functional PIC chip. Thus, the total manufacturing cost per each functional PIC chip can be represented as: total cost = (((a) + (b)) x (c)). Therefore, one need to minimize the substrate and fabrication costs and maximize the integration densities of the devices layout in order to get the minimum costs of the PIC chips. However, the cost of substrates is largely determined by the commercial market.

As an example, silicon wafers are much cheaper than III-V semiconductor wafers as the microelectronic industry is dominant by silicon.

Table 1.4 lists the comparison of wafer costs of various kinds of semiconductor wafers. The largest available wafer sizes in both R&D and commercial markets are also listed.

	Wafer sizes (R&D)	Wafer sizes (commercial)	Wafer costs (USD)	Substrate costs per 1mm^2 (USD)
Silicon	450 mm	300 mm	150	0.0015
Silicon-on-insulator	450 mm [17]	300 mm	1200	0.012
Indium phosphide	150 mm	100 mm	450	0.045
Gallium arsenide	200 mm	150 mm	450	0.02

Table 1.4. Comparison between various cost of semiconductor wafers

The substrate cost per area for SOI wafers is half of GaAs wafers and one third of InP wafers. In addition, the fabrication cost in SOI is also way cheaper than in III-V counterparts by taking advantages of mature CMOS fabrication process and well-developed facilities. For point (c), in order to maximize the integration density, the primary limitation is on the refractive index of core and cladding of optical waveguides. Fundamental waveguide principle shows that the higher refractive index difference between the core and cladding (Δn) would enable higher confinement of optical mode in the core region, finally enables smaller size of optical waveguides and smaller bending radius. The smaller size and bending radius thus allow a higher integration density,

therefore the integration density of a PIC can be accessed by the ratio of Δn/n.

	Wavelength (mm)	Refractive index n	Band gap	Δn/n (%)	T/O coef. dn/dT (K^{-1})
Silicon-on-insulator	1.1	3.5	Indirect	60	1.86×10^{-4}
Indium phosphide	1.55	3.1	Direct	0-3	0.8×10^{-4}
Gallium arsenide	0.8	3.4	Direct	0-14	2.5×10^{-4}

Table 1.5. Comparison among SOI and III-V semiconductor PIC platforms

Table 1.5 shows the comparison among SOI and III-V semiconductor including InP and GaAs [2]. Due to the large refractive index difference between Si (3.5) and the cladding silicon dioxide SiO_2 (1.5), the Δn/n of the SOI PIC platform can be as high as 60%, which is significantly higher than in InP (3% (channel)) and GaAs (14% (rib)). Today's single-mode optical waveguides in SOI platform has a typical dimension of 500 nm width and 220 nm height. This sub-micron 'nanowire' waveguide provides ultrahigh integration density compared with III-V semiconductors.

From the above analysis, SOI platform provides all the cost advantages than III-V semiconductor platforms in substrate costs, fabrication costs and integration density. The cost advantages of SOI platform is thus a great advantage of silicon photonics to accomplish the goals of optical interconnects.

1.3 Optical resonators

Optical resonators are optical structures that confine light into the structures (cavities) for certain optical wavelength/frequency. As the field of optics advances, optical resonators can be constructed in many different configurations. In free-space optics, the most common types of optical resonators consist of two plane mirrors that facing each other as shown in Fig. 1.5. This structure is also known as a Fabry-Perot resonator.

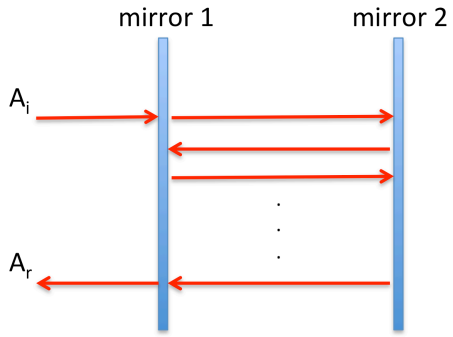

Fig. 1.5. Schematic of the Fabry-Perot resonator. Mirror 1 has non-zero reflectivity and mirror 2 is a perfect mirror.

In the structure shown in Fig. 1.5, mirror 1 has non-zero reflectivity and mirror 2 has 100% reflectivity. The incident beam (with amplitude of A_i) is partially transmitted to the cavity through mirror 1. The mirrors reflect the transmitted light for couple times inside the cavity. The round-trip phase difference ($\boldsymbol{\delta}$) between the successive waves is $\boldsymbol{\delta} = 4\pi n\mathbf{d}/\lambda$, where n is the refractive index of the cavity medium, **d** is the separation of the mirrors and λ is the wavelength of light in vacuum. The reflection intensity $R = |Ar/Ai|^2$ is at resonance when $\delta = 2m\pi$, where Ar is the amplitude of the reflected beam and m is an integer. Therefore, the resonance condition can be written as

$$\lambda_m = 2nd/m, \tag{1.1a}$$

where λ_m is the m order of the resonant wavelength.

And the resonant wavelengths are separated by

$$\Delta\lambda \sim= \lambda^2/2n_g\mathbf{d} \quad (1.1b)$$

where $\Delta\lambda$ is the free spectral range (FSR), λ is the average of two resonant wavelengths, and n_g is the group index of the cavity. The corresponding group index $n_g = n - \lambda(\delta n/\delta\lambda)$.

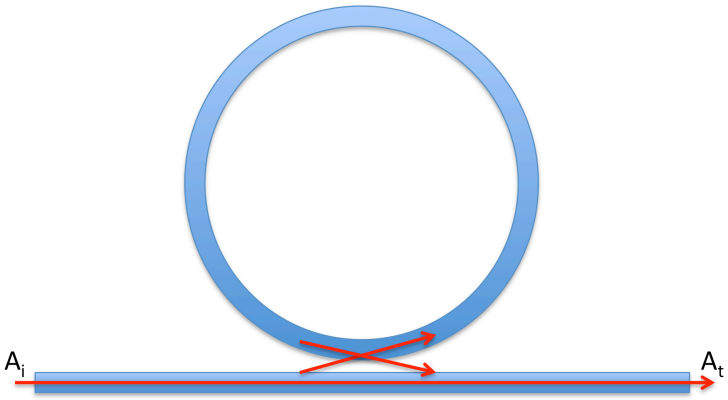

Fig. 1.6. Schematic of the ring resonator. Light coupled to the ring resonator by evanescent coupling from the coupling waveguide.

Fig. 1.6 shows the schematic of a standard ring resonator coupled with a waveguide. The circumference of the ring is **L**. The principle of ring resonator is very similar to the Fabry-Perot etalon as shown in Fig. 1.5, as light are confined in the cavity (ring) as they travel along the ring for many cycles. Therefore, the resonance condition and the FSR by replacing the cavity length of 2d in equations (1.1a) and (1.1b) by circumference **L**:

$$\lambda_m = n\mathbf{L}/m \quad (1.2a)$$

$$\Delta\lambda \sim= \lambda^2/n_g\mathbf{L} \quad (1.2b)$$

In optical resonator, a key figure-of-merit is quality factor (Q). Quality factor is the measured by energy capacity of the optical resonator, it defines as:

$$Q = \omega\tau = (2\pi c/\lambda)\tau \quad (1.3)$$

where ω is the frequency, λ is the resonance wavelength, c is the speed of light in vacuum and τ is the photon lifetime. We can also obtain the quality factor by transmission spectrum in frequency or wavelength domain as:

$$Q = \omega/\Delta\omega = \lambda/\Delta\lambda \tag{1.4}$$

where λ is the resonant wavelength and $\Delta\lambda$ is the full-width at half-maximum (FWHM) of the resonance dip/peak.

1.4 Photonic crystals

Photonic crystals (PhCs) are artificially created materials in which the refractive index varies periodically between high-index regions and low-index regions [18]. The periodicity can be in one, two or three dimensions. Under certain conditions, this periodicity results in coherent scattering of electromagnetic wave as it propagates through the PhCs, and a complete photonic bandgap (PBG) opens. Light for any wavelength within the PBG is prohibited for propagation. Therefore, a PhC can be used as a reflector for wavelengths that fall within the PBG. The principle is analogous to that in a semiconductor crystal, where a periodic arrangement of atoms presents a periodic potential to an electron propagating through it. Thus prohibits the propagation of certain waves and forms an electronic band gap.

The study of photonic crystals was actually more than a hundred years ago. In 1887, Lord Rayleigh published one of the earliest analyses of optical properties of multilayer films, which is a 1-D photonic crystal. This specific type of photonic crystal can act as a mirror (a Distributed Bragg Reflector (DBR)) for light within wavelengths fall in the PBG. In 1987, Eli Yablonovitch and Sajeev John published two milestone papers concerning about high dimensional periodic optical structures [19, 20], and they created the term “photonic crystals”. In 1991, Eli Yablonovitch demonstrated the first 3-D photonic band-gap [21]. However this demonstration is in microwave regime rather than in optical wavelength, most likely due to difficulties in fabrication of device dimensions in optical scale. In 1996, Tomas Krauss made the first demonstration of 2-D PhCs at optical wavelength [22]. This type of 2-D slab PhCs has been studied extensively due to its excellent compatibility of PIC fabrication process. Figure 1.7 shows the scanning

electron microscope (SEM) images of the planar photonic crystal defect waveguides on SOI and InP substrate [23,24]. Adding a defect into the PhCs is similar to the doping process in semiconductor. In [23,24] the line defects have been added into 2-D PhC lattices to form PhC waveguides. PhC waveguides guide light by total internal reflection above and below the slab while the 2-D PhCs around the defect lines act as all-direction reflectors in the plane of propagation. By similar concept, one can add a point defect to the PhCs to form low modal volume cavities as PhC resonators [25].

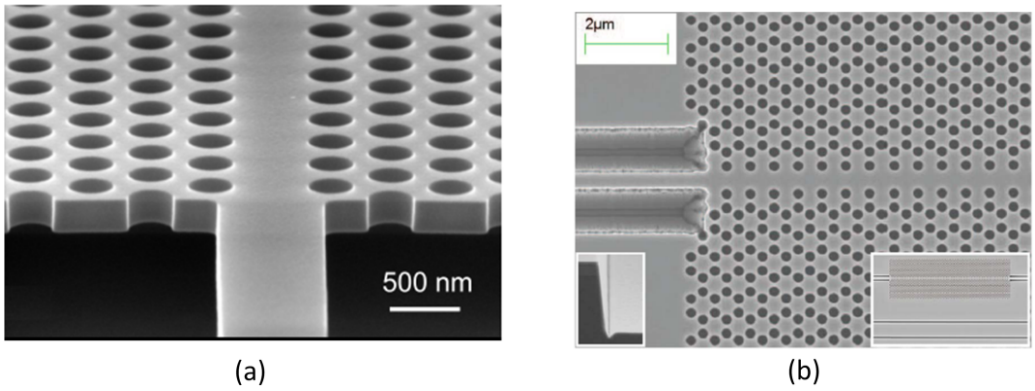

Fig. 1.7. (a) SEM image of silicon based photonic crystal defect waveguide reported in [23]. (b) SEM image of indium phosphide based photonic crystal defect waveguide reported in [24].

One of the most important features of PhCs is its dispersion characteristic. PhCs enable a large PBG when the refractive index contrast between high-index regions and low-index regions are high. It can be achieved in typical 2-D slab PhCs in SOI or InP material platform. In where the high-index regions are Si/InP (index of ~3.5) and the low-index regions are usually air (index of ~1). This large PBG introduces a strong optical dispersion close to the band-edge. The strong optical dispersion leads to "slow-light" effect, as the group velocity $v_g = \delta w/\delta k$ tends to zero at the band-edge [26]. By combing with dispersion engineering [27-28], the "slow-light" effect offers numerous applications

such as optical buffering, time-domain processing and nonlinear optics performance enhancement.

PhCs offer unprecedented opportunities for molding the flow of light by creating defects, dispersion engineering and “slow-light” effect. By combing the fabrication advantages in silicon photonics and optical characteristics of PhCs, silicon based PhCs have been used in last decade to demonstrate various high performance devices such as optical delay lines [29], high quality factor micro-cavities [30] and small modal volume cavities [31]. And lead to applications range from optical biosensing [32] to low-energy optical modulators [33].

1.5 Thesis objectives

This thesis describes how we design, fabricate and characterize silicon photonics based ring-shaped photonic crystal structures. These devices combine microring structures with PhC waveguides and PhC nano-cavities, in order to provide enhanced optical characteristics. These optical characteristics thus lead to the demonstration of couple of applications on the field of label-free biosensing and optical-interconnects. These ring-shaped silicon photonic crystal nano-photonic devices, as shown in the remaining of the thesis, could open the door for numerous of applications such as optical signal processing, low energy optical modulation and lab-on-a-chip biosensing.

1.6 Thesis outline

This thesis is divided into seven chapters. Chapter 1 is an overall introduction of the photonic device researches including the introduction of background and applications of the photonic devices, the objectives of the thesis and the structure of the thesis. Chapter 2 provides the details of research methods applied in this thesis. Chapter 3 presents the research results of biosensing experiments by employing photonic crystal microring resonators. Chapter 4 presents a novel method of Bloch modes selection by using photonic crystal microring resonators. Chapter 5 shows the demonstrations of a broad-band coupling method to highly dispersive resonators. Chapter 6 presents a novel device of embedded one-dimensional photonic crystal cavity, with its potential applications for optical-interconnects. Chapter 7 summarizes the thesis and discusses the future work.

2. Methods

In this chapter, the details of methods employed throughout the thesis will be presented. Figure 2.1 shows the flow of nano-photonic device researches. It starts from fundamental theory, to simulation and design, then finally device fabrication and finally device characterization. Usually this linear research flow just indicates one cycle in the whole project, as some error or unexpected results may occur at some points of the procedure in the flow. For example, a fabrication error in the etching process during the device fabrication step may cause an undesired deice dimensions that result in unexpected results in experiments. In order to find out the 'mismatch' between unexpected experimental results and theoretical predictions/simulation results, a 'debugging' process will be employed, it usually by the mean of extended simulation and post-fabrication device metrology. Therefore, in each of projects (chapters) presented in this thesis, the actual research flow usually contains few (3-6) cycles of process flow for simulation-fabrication-characterization, in order to fine tuning all the steps to achieve satisfied experimental results. In the following sections, the details of device simulation, fabrication and cauterization will be presented and explained.

Fig. 2.1. Research flow of nano-photonic device researches. The flow starts from fundamental theory, to design and modeling, then finally device fabrication and device characterization.

2.1 Device simulation

Device simulation is a key process during the device research process flow, as it defines how do we design the device structures and provide us insight on why do we choose the structures. Therefore, device simulation serves three major purposes: (1) obtain device design parameters, (2) provide theoretical optical characteristic of simulated photonic devices and (3) verifying the experimental results and compliment the experimental results with data could not obtain experimentally (like optical mode profile with nanometers resolution). In this thesis, the simulation methods of finite difference time domain (FDTD) is extensively used as it provides excellent predictions on photonic crystal (PhC) based nano-photonic devices. Planewave expansion (PWE) method has also been employed in some of chapters to calculate the photonic band diagram. Their principles will be presented in followings.

2.1.1 Finite difference time domain method

In 1966, Kane Yee introduced FDTD method [34], in order to obtain the numerical solution of Maxwell's equations. The FDTD method solves Maxwell's equations by discretizing the equations via central differences in both time and space domains. The method computes the electric and magnetic field components at the grid points based on the mesh setting of Yee cell, with grid point spacing of Δx, Δy and Δz. Figure 2.2 shows the schematic of the Yee cell with dimensions of Δx, Δy and Δz. The magnetic field components are computed at points shifted by half of grid size from the electric field grid points.

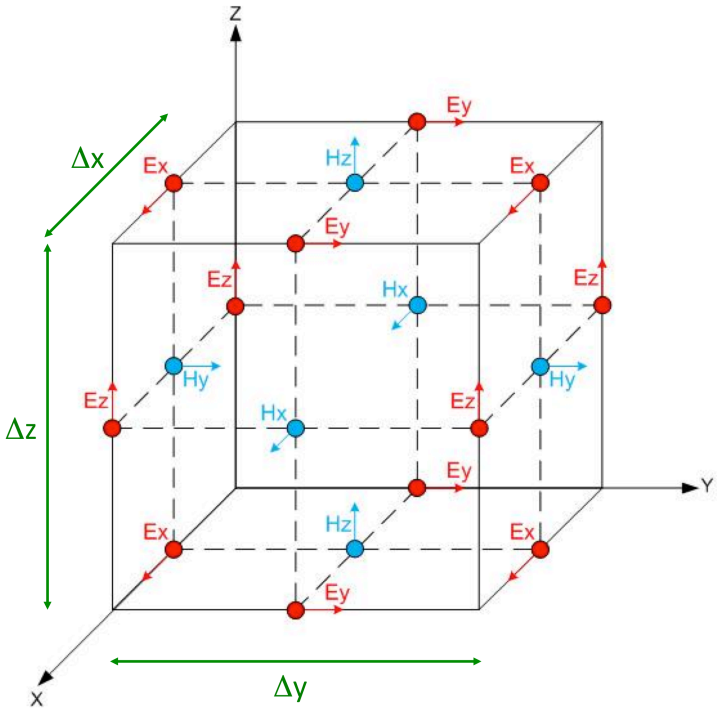

Fig. 2.2. Schematic of the Yee cell with dimensions of Δx, Δy and Δz. [modified from 35]

In order to obtain stable simulation results, the courant condition has been met. The courant condition relates the spatial and temporal step size in the simulation by:

$$c\Delta t < \frac{1}{\sqrt{\left(\frac{1}{\Delta x^2}+\frac{1}{\Delta y^2}+\frac{1}{\Delta z^2}\right)}} \tag{2.1}$$

where c is the sped of light in free space, Δx, Δy and Δz are spatial grid sizes in x, y and z directions. In the FDTD simulation, the computation domain boundaries are assigned as perfectly-matched layer (PML). The PML boundary condition act as an extremely lossy boundary that in principle would only absorbs/transmits light that pass through this boundary without any reflections. In this thesis, the commercially available software

package of Lumerical FDTD solutions [36] has been used for all projects for device simulations.

2.1.2 Planewave expansion method

For periodic structure, like photonic crystal, PWE method would be the ideal simulation technique for calculating the photonic band diagram. PWE method computes definite-frequency eigenstates of Maxwell's equation in periodic dielectric structures for arbitrary wavevectors, using fully-vectorial and 3-D methods [37]. It expands the electric and magnetic fields in terms of Fourier series components, then do a direct calculation of the eigenvalues of the Helmholtz equation by iterative technique. It is limited by the assumption of symmetric boundaries. In this thesis, the open-source software package of MIT Photonics-Bands (MPB) [38] has been used for projects that required photonic band diagram simulations. The MPB software was developed by Prof. Steven G. Johnson from MIT and 1990s and released to public in 1999 to facilitate the research on PhC.

2.2 Device fabrication

Device fabrication is another important step during the device research process flow, as it defines the dimensions of actual fabricated device structures. Ideally the fabricated device should be identical to the designs that finalized in the design and modeling stage. However, due to the limitation of fabrication in every fabrication steps, some biasing condition and design of experiments may be required for achieving desired results at the end. Therefore, understanding thoroughly about the fabrication limitation and expectation would be important for photonic device researches. The detailed device fabrication process is shown as follows, the processes were done in the Center for nanophase material sciences (CNMS), Oak Ridge National Laboratory (ORNL) [39] and Georgia Tech Institute for Electronics and Nanotechnology [40].

Commercial silicon-on-insulator (SOI) wafers from SOITEC [41] with a 270nm device layer on top of a 3μm buried oxide (BOX) layer were used for the device fabrication. Dry-oxidation and a subsequent dip in buffered oxide etch (BOE) were performed to thin down the top silicon layer to the desired thickness of 220nm. The nano-photonic devices were then patterned on the SOI chip using a single step of electron beam lithography (EBL) and a reactive-ion-etching (RIE) process.

Figure 2.3 shows the schematic of the device fabrication process flow of single step of EBL and RIE process. First, a high-resolution positive-tone electron-beam photoresist (ZEP 520A) was first spin-coated on the wafer at 6000rpm for 45 seconds, which resulted in a resist thickness of ~300nm. Second, following a soft-bake at 180°C for 120 seconds on a hotplate, the design patterns were exposed using a JEOL JBX-9300FS EBL system. The typical dosage used for EBL exposure is 300-340 $\mu C/cm^2$. Depending on the pattern

of nano-photonic devices, proximity effect correction (PEC) technique may be employed during the EBL process. In which the dosages of different area of the pattern were altered to compensate the proximity effect of electron forward and backward scatterings. After the exposure, the wafer was developed by Xylenes for 30 seconds and rinsed by IPA for 30 seconds. Nitrogen blow-dry was used to dry the surface. The wafer was then dry etched for ~2 minutes using a SF_6-based inductively-coupled-plasma (ICP) RIE etcher Oxford Plasma Lab 100, with a top silicon etch rate of 1100-1500Å/minute. Usually the etch rate of silicon etching would be calculated by a dummy wafer run of same etching recipe of 2minutes run. Surface profilometer was used to measure the etch depth thus obtaining the etch rate. Finally the remaining photoresist on the wafer was removed by O_2 plasma in the same chamber for ~1 minute. After the fabrication, the devices were inspected by scanning electron microscope (SEM) tools immediately to verify the dimensions of fabricated structures.

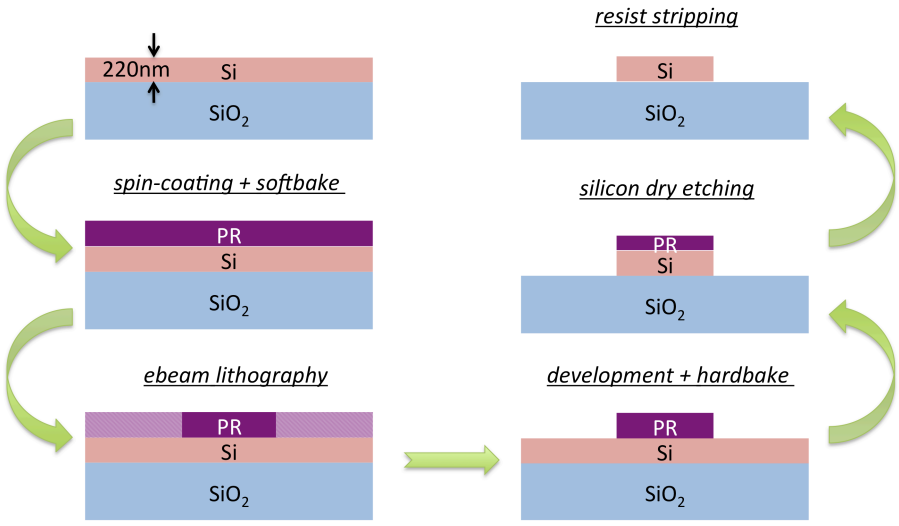

Fig. 2.3. Schematic of the typical fabrication process flow for nano-photonic devices. The silicon substrate under the buried oxide layer is not shown in the picture. PR: photoresist.

2.3 Device characterization

Device characterization is the final step of the research flow. It means to obtain the optical properties of the fabricated photonic devices by different experimental methods. In this thesis, the most important optical property of photonic devices is their transmission spectra. Transmission spectra provide the information of optical losses, wavelength responses and other important figure-of-merits like quality factor and extinction ratio of optical resonators. In this thesis, transmission spectra were measured using a wavelength scanning technique.

Figure 2.4 shows the photograph of the experimental setup used to couple light of the light source into the device under test (DUT) and couple light out from the DUT to the detector. An external-cavity continuous-wave (CW) tunable semiconductor diode laser (Santec TSL-510) was used with a wavelength tunable range from 1510nm to 1630nm. The output laser beam was guided by a single-mode optical fiber (SMF) to a polarization controller to adjust the output polarization. The output polarization was transverse electric (TE)-like in all experiments and was calibrated using a free space polarization beam-splitter and photodetector. The laser beam was then coupled to the device through a 10° tilted cleaved-end SMF and an input grating coupler on the sample that was fabricated alongside the photonic devices. The grating coupler design reported in [42] was followed with appropriate modification of the dimensions for devices on 220nm thick SOI. The output signal from the output grating coupler was collected by a cleaved-end SMF. The positions of the SMFs and sample were controlled by translation stages. A long working distance lens and visible-light CCD camera on top of the sample monitored the alignment of the sample and fibers. In some of experiments, the long working lens

was connected to a beam-splitter and an infrared camera was used to collect the out-of-plane scattering images of the photonic devices. The transmission intensities were measured by a photodetector and recorded by a fast speed data acquisition (DAQ) system. The DAQ system provides highest measurement rate of 1MHz, while the usual measurement rates used in our experiments were 1kHz and 10kHz. As the wavelength sweeping speed of the tunable laser was 5nm/s, the 1kHz measurement rate provided 5pm resolution, and the 10kHz measurement rate provided 0.5pm resolution.

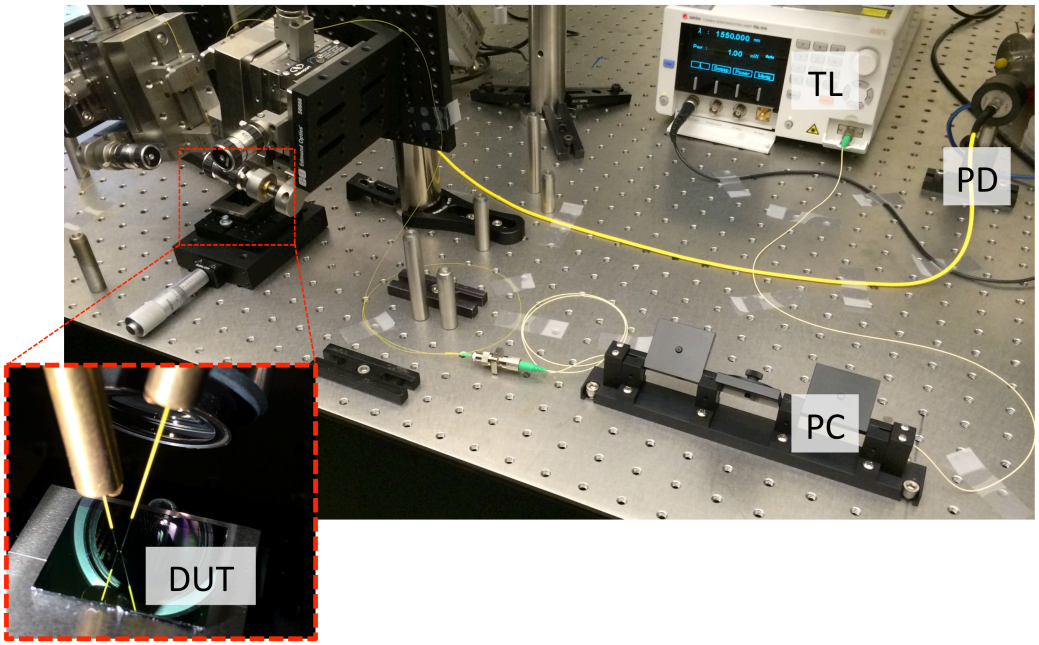

Fig. 2.4. Photograph of the experimental setup used to couple light in-to/out-of the photonic devices. In the optical system, the light source is the tunable laser and the detector is the photodiode. TL: tunable laser. PD: photodetector. PC: polarization controller. DUT: device under test.

3. Photonic crystal microring resonator for label-free biosensing

In this chapter, a label-free optical biosensor based on a one-dimensional photonic crystal microring resonator with enhanced light-matter interaction is demonstrated. More than a 2-fold improvement in volumetric and surface sensing sensitivity is achieved compared to conventional microring sensors. The experimental bulk detection sensitivity is ~248nm/RIU and label-free detection of DNA and proteins is reported at the nanomolar scale. With a minimum feature size greater than 100nm, the photonic crystal microring resonator biosensor can be fabricated with the same standard lithographic techniques used to mass fabricate conventional microring resonators.

3.1 Background

In the last decade, on-chip optical label-free biosensors based on optical resonant cavities have drawn a great deal of interest for delivering fast, portable, cost-effective, sensitive and accurate diagnostics [43-52]. Label-free biosensors promote simple analyte preparation and real-time monitoring of specific binding interactions by transducing the presence of specific target molecules based on their capture by surface immobilized bioreceptors, as opposed to traditional methods of labeling the target analytes with fluorescent or radiative tags [53]. Furthermore, silicon-based biosensors using the silicon-on-insulator (SOI) platform have the advantages of (1) strong light-matter interaction between resonant modes and target analytes, which increases detection sensitivity, and (2) compatibility with CMOS fabrications processes, which facilitates low-cost, compact and high quality photonic devices. Various types of optical resonant structures in silicon

have been proposed and demonstrated as optical label-free biosensors such as microring resonators [43-46], one-dimensional (1D) photonic crystal (PhC) cavities [47] and two-dimensional (2D) PhC cavities [48-52]. Numerous device design approaches have been employed to further improve the sensitivity of biosensors by enhancing the light-matter interaction between target analytes and optical mode field of resonant cavities. These approaches include slot waveguide-based microring resonators [54], suspended micro-ring resonators with an enhanced evanescent field [55], sub-wavelength grating based microring resonators [56], multi-hole defect PhC micro-cavities [57], slotted PhC cavities [58] and high-Q PhC cavities [59].

In this chapter, a PhC microring resonator (PhCR) [60-63] is demonstrated as a label-free biosensor for specific molecular detection with enhanced detection sensitivity due to its strong light-matter interaction that results from the localized optical mode field profiles of the PhC structure. Since a fraction of the optical field in the PhCR is located inside the air holes that are accessible for molecular attachment, the PhCR can detect the presence of analyte both inside the holes and on the top surface. Importantly, in contrast to slots and multi-hole defects that also support increased light-matter interaction for sensing, the critical dimensions of PhCRs are compatible with advanced deep ultra-violet (DUV) lithography [63,64], which could lead to the production of high-volume, low-cost lab-on-a-chip biosensors. Moreover, all of the important properties of conventional microring resonators as biosensors are preserved for PhCRs while a significant challenge for sensing high concentrations of molecules is removed. Like conventional microrings, PhCRs can be easily coupled to a silicon bus waveguide, enabling low optical loss, formation of sensor arrays, and error-correcting capabilities [65]. In addition, PhCRs do

not have an upper limit on the concentration of analyte that can be detected due to their photonic bandgap (PBG) that gives rise to aperiodicity in the transmission resonances; the periodic transmission resonances of traditional ring resonators lead to ambiguity when measuring large spectral shifts that exceed the free spectra range. Based on the aforementioned attributes, PhCRs are promising candidates for highly sensitive biosensors in future on-chip diagnostic devices. Although the application of PhCRs as bulk refractive index sensors has been studied experimentally [66,67] and theoretically [68,69] in a few different geometries, its surface sensing capabilities have yet to be demonstrated. As a critical step toward molecular diagnostic applications, it is important that label-free biosensing experiments are shown on the PhCR platform. Moreover, previously demonstrated PhCR structures with shallow-etched holes or grating designs exhibit bulk detection sensitivities of <100nm/RIU [25,26], which are lower than those of conventional microring based sensors [43]. Therefore, in this chapter, an optimized PhCR structure with stronger light-matter interaction is presented in order to demonstrate that PhCRs can achieve superior sensing performance over conventional microring resonators in both volumetric and surface sensing experiments. In the following sections, the device structure, experimental methods, and results on bulk refractive index sensitivity and label-free biosensing of DNA and protein will be presented.

3.2 Device structure

3.2.1 Photonic crystal microring resonator

Figure 3.1(a) shows the top-view scanning electron microscope (SEM) image of the PhCR. The structure is fabricated on a SOI platform with a 220nm thick device layer. The silicon layer is etched through to the buried oxide layer. There are **N** = 100 circular air holes on the ring resonator, resulting in a ring radius of ~7.16μm. Figure 3.1(b) shows the magnified top-view SEM image of the device at the coupling regime. The periodicity of the air holes is **a** = 450nm, the hole radius is **r** = 0.3**a** = 135nm, the width of the ring is **d** = **a** = 450nm. The width of the coupling waveguide is **w** = 0.8**a** = 360nm or **w** = 0.75**a** = 338nm, both of which led to excellent mode matching between the input waveguide and PhCR [60]. The gap separation is **g** = 0.3**a** = 135nm, **g** = 0.4**a** = 180nm or **g** = 0.6**a** = 270nm. All of these gap separations were close to critical coupling and thus yielded high extinction ratios of the resonances. Figure 3.1(c) shows the magnified top-view SEM image of the device at the arc of the PhCR. In the SEM image, pattern distortion such as irregular air-holes is observed, this could due to fabrication imperfection like proximity effect during EBL process. The irregular air-holes could add additional loss to the PhCR structure hence reduce the quality factor.

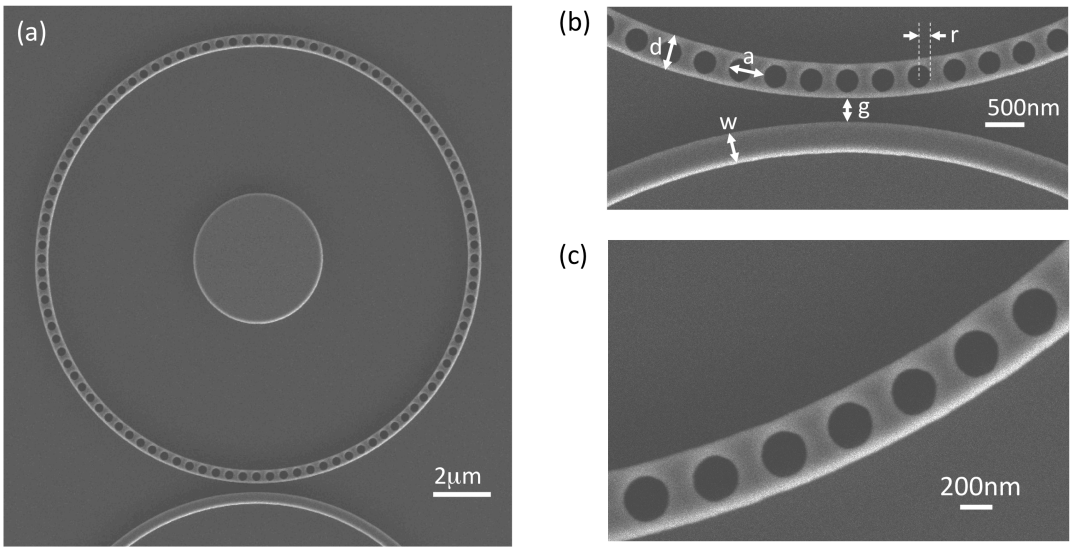

Fig. 3.1. (a) Top-view SEM image of the fabricated photonic crystal microring resonator. (b) Magnified top-view SEM image of the coupling region of the PhCR. (c) Magnified top-view SEM image of the PhCR, pattern distortion is observed due to fabrication imperfection.

3.2.2 Control devices

In order to give a fair comparison of sensing performance between PhCRs and conventional microring resonators, the dimensions of the fabricated control microrings are largely the same as the PhCR. The ring radius of the control microring is ~7.16μm. The width of the control microring is 450nm. The width of the coupling waveguide to the control microring is also 450nm. The gap separation between the coupling waveguide and the control microring is 100nm. The control devices are fabricated with PhCRs on the same die at a close proximity and undergone exactly the same fabrication process. During the stage in the biosensing experiment, this makes sure both PhCRs and control devices will have very similar condition that would be critical for the sensing results such as temperatures and bio-molecules coverage.

Additional devices such as microring resonator with width of 500nm and 400nm have also been designed and fabricated on the same die. These structures are used to compare with the control devices in both bulk sensing and surface sensing experiments. As the sensor performance should inversely proportional to the width of microring resonators, due to the higher portion of evanescent field into the air of a narrower width waveguide. The experimental results match with what one would expect with almost perfect consistency in bulk sensing and every step of DNA and protein sensing experiments. This provides another experimental verification that the results on PhCR devices are highly reliable throughout the whole experimental process.

3.3 Simulation results

3.3.1 Optical mode profiles

Figure 3.2(a) shows an example of the on-resonance optical mode field profile of the PhCR. Figure 3.2(b) shows the magnified optical mode field profile of the PhCR in a section of the PhC waveguide. The profile is calculated using three-dimensional (3D) finite-difference time-domain (FDTD) analysis [36]. Dimensions of the device used in the simulation are similar to the fabricated devices. The interface between Si and air regions in the PhCR structure is shown as a solid white line. The resonance wavelength is close to the photonic band gap of the structure. The polarization is TE-like (electric field parallel to the device plane).

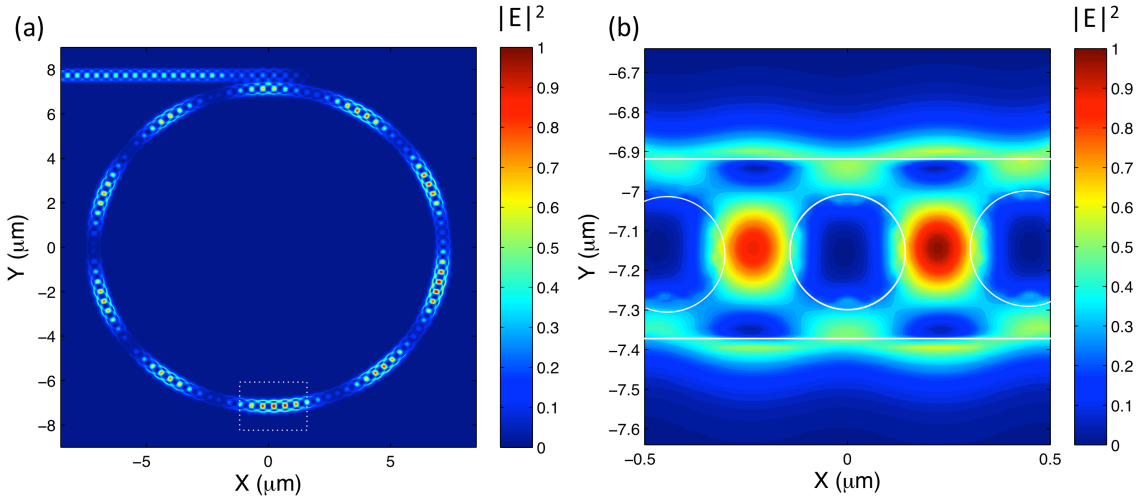

Fig. 3.2. (a) FDTD calculated optical mode profile when the photonic crystal microring resonator is on-resonance. (b) Magnified optical mode field profile of the PhCR in a section of the PhC waveguide, which shows that a fraction of the optical field is located at the edge of air holes.

As shown in Fig. 3.2(a), a strong beating pattern occurred in the resonance mode of the PhCR structure. This beating pattern, created by the forward propagating and backward

propagating modes in the resonator due to the strong coupling among them, is an important optical characteristic in the PhCR. As in usual microring that formed by a standard silicon waveguide, the optical mode at resonance will be uniform across the ring. Although this macroscopic mode pattern would not contribute to the enhancement (or reduction) of sensing performance of the PhCR, it could leads to some novel applications such as on-chip multi-wavelength routing as an add-drop filter. The details will be discussed in chapter 4.

3.3.2 Enhanced light-matter interaction

The potential of using the PhCR as a superior bio-sensor over conventional microring resonator is due to its microscopic optical mode distribution rather than its macroscopic one. From Fig. 3.2 (b), the mode profile indicates most of the optical energy is localized in the silicon region, as the resonance wavelength sits near the dielectric band edge. However, the evanescent field of the localized mode still extends to the surrounding air holes and provides enhanced modal overlap between the optical mode and the inner surface of the air holes where biomolecules can be attached. This additional active sensing area leads to an enhancement in sensitivity for PhCR as optical biosensors compared to conventional microring devices.

With this potential enhancement in mind, bulk index sensitivity simulations based on 3-D FDTD have been performed. A sensitivity of ~190nm/RIU of PhCRs have been calculated by modifying the refractive index of upper claddings above the BOX layer. Which is about two times higher than conventional microring device with same width.

Note that in the fabrication process, EBL overdosing and enlarging air-holes and narrower waveguide widths are very typical, thus an even higher experimentally measured sensitivity would be expected.

3.4 Surface functionalization methods

3.4.1 DNA molecules

For experimental demonstration of surface-based DNA label-free biosensing, a protocol similar to that reported in [70] was followed to attach DNA to the PhCR. First, the sample was oxidized in air at 500°C for 10 minutes to ensure that the appropriate surface passivation and surface chemistry was obtained for subsequent functionalization steps. Next, 3-aminopropyltriethoxysilane (3-APTES) was diluted in anhydrous toluene to a concentration of 2%, and the sample was soaked in the resulting solution for 15 minutes to achieve an amine terminated surface functionalization. Thereafter, the sample was flushed with ethanol and DI water several times and cured inside an oven at 150°C for 20 minutes. A linker molecule, succinimidyl 3-(2-pyridyldithio)propionate (SPDP), was dissolved in HEPES buffer, and the sample was then soaked in the solution for 2 hours, followed by a 1 hour HEPES buffer soak to remove any unbound molecules. An excess (100μM) of 16-mer probe DNA in HEPES buffer was mixed 1:1 by volume with disulfide reducing agent TCEP in DI water and ethanol for 30 minutes and then pipetted onto the sample. After 1 hour incubation at 37°C, the sample was soaked in HEPES buffer for 20 minutes at 37°C, rinsed with DI water, and dried with nitrogen gas to remove any remaining unattached molecules. Finally, a 16-mer single-stranded target

DNA at a concentration of 500nM was attached to the sample. We note that the PhCR and control microring devices were exposed to identical functionalization processes and experimental conditions for all experiments to enable a direct comparison of their biosensing performance.

3.4.2 Protein molecules

For the experimental demonstration of label-free protein detection, the following protocol was followed to attach proteins to the PhC microring biosensor. First, the oxidized samples were immersed in a freshly prepared piranha solution for 15 minutes to remove organic surface contaminants and ensure a chemically clean surface. Following piranha clean, the samples were rinsed thoroughly with copious amounts of water and dried under nitrogen. Then, 50μL of freshly prepared 2% 3-APTES solution in anhydrous toluene was drop cast onto each sample for 15 minutes to provide an amine functionalized surface. The excess unreacted 3-APTES was thoroughly rinsed from the samples three times with ethanol and DI water. The samples were then dried under nitrogen flow and baked in an oven at 100°C for 20 minutes to enable the formation of stable 3-APTES cross-links. Next, 50μL of a 200μM biotin solution in phosphate buffer saline (PBS) buffer was pipetted onto each sample and incubated for 1 hour. Unattached biotin molecules were washed away by rinsing the samples with DI water and ethanol, then drying under nitrogen. The samples with covalently bound biotin probe molecules were then sequentially exposed to 50μL of varying concentrations (20nM, 100nM, 200nM) of target streptavidin molecules solvated in PBS solutions for 1 hour. Excess streptavidin

molecules were washed away from the sample surface by thorough DI water and ethanol rinse steps. The samples were then dried under nitrogen. Note that for all experiments, the same sample was exposed to increasing streptavidin concentrations without removing the already captured streptavidin molecules.

3.5 Experimental results and discussion

3.5.1 Bulk index sensitivity

Figure 3.3(a) shows a typical transmission spectrum of the PhCR-based biosensor. The wavelength resolution is 5pm. The incident power is fixed at 1mW for all experiments. In the spectrum, there are no resonances below about 1550nm due to the PBG. Above 1550nm, there are multiple resonance dips with highly non-uniform free spectral ranges (FSRs). The FSR between resonance peaks decreases from ~12nm at ~1595nm to ~3nm at ~1555nm. The reduction of FSRs close to the band-edge of the PBG is due to the slow-light effect of the PhC waveguide embedded in the microring. The calculated group index is ~17 ($\mathbf{n_g} \approx l^2/dlL$ where L is the circumference of the PhCR). For the control microring resonator, the FSR between resonance peaks is ~11.5nm across the entire optical spectrum. This uniform FSR shows a linear dispersive characteristic, and the calculated group index is ~4.6 at 1555nm. Note that the slow light effect for the PhCR does not directly contribute to its increased detection sensitivity because the increased group index results in both an increase of the phase change in the PhCR and a decrease in the FSR. The extinction ratio of the resonance mode in the PhCR next to the photonic band edge is ~10dB, which suggests a nearly critical coupling condition of the resonator is achieved.

However, the loaded quality factor Q_{load} of the same mode is ~1200, which is less than that of our previously fabricated PhCRs (Q_{load} ~ 2500) [60]. The lower Q_{load} of this PhCR compared to previously fabricated PhCRs may be due to fabrication imperfections and enlarged air hole dimensions in these specific devices for biosensing applications. The enhanced modal overlap at the silicon-air interface also increases the magnitude of scattering losses that result from surface roughness produced during the silicon reactive ion etching process in the fabrication. The control mircroing exhibits a loaded quality factor of ~35,000 and an extinction ratio of ~15dB for the resonance at 1555nm.

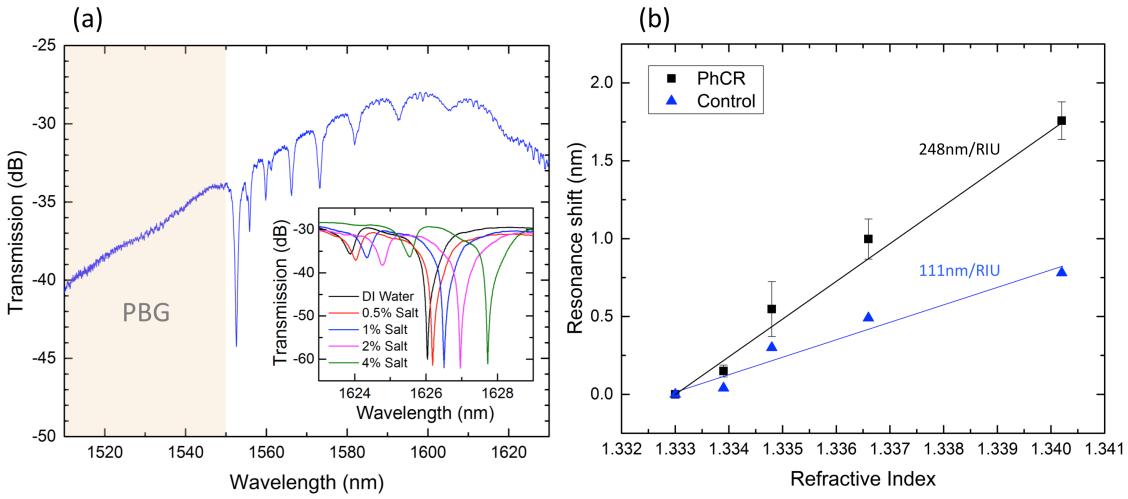

Fig. 3.3. (a) Measured TE-polarized transmission spectrum of the PhCR. PBG: photonic band gap. (Inset) Measured transmission spectra of PhCR exposed to DI water and different concentrations of salt water solution. Resonances are red shifted when salt concentration is increased. (b) Resonance shifts of PhCR and control microring exposed to different concentrations of salt water solution. The solid lines are linear fits to the data.

In order to obtain the bulk refractive index sensing performance of the PhCR, the PhCR along with a conventional microring resonator were exposed to salt water solutions with different NaCl concentrations. In the experiment, 0%, 0.5%, 1%, 2% and 4%

concentration solutions were used. The transmission measurements of the PhCR and control microring devices were immediately started once the solutions were applied on the sample. The samples were rinsed by DI water and dried with nitrogen gas between measurements, before the next salt water solution was exposed to the samples. After rinsing, the resonance wavelength returned to its initial condition, confirming that no salt residue remained in the samples. The inset of Fig. 3.2 (a) shows the measured transmission spectra of the PhCR exposed to DI water and different concentrations of salt water solution. The results indicate the resonance dips red shift when salt concentration is increased. Figure 3.3 (b) summarizes the resonance shifts of the PhCRs and control, conventional microring resonators as a function of the refractive index of the applied salt water solution. Linear fits to the data show that the PhCR has an experimental bulk refractive index sensitivity of ~248nm/RIU, while the control microring has a sensitivity of ~111nm/RIU. Note that the bulk sensitivity of the control microring is similar to what has been previously reported [43]. The more than 2-fold increased bulk detection sensitivity of the PhCRs compared to the control microring is largely due to the increased area for light-matter interaction between the guided mode and salt water solution exposed to the rings.

3.5.2 Label-free biosensing of DNA molecules

In order to examine the surface-sensing capabilities of the PhCR, label-free biosensing experiments were first carried out using the specific attachment of DNA molecules. Figure 3.4 (a) shows the measured TE-polarized transmission spectra of the PhCR after each step of the surface functionalization processes and after capture of the target DNA molecules. After oxidation of the sample that blue shifts the resonance (not shown), the resonance wavelength red shifts after each molecular attachment step as a thin layer of biomolecules functionalized on the PhCR surface increases the effective refractive index of the PhCR. Figure 3.4 (b) summarizes the resonance wavelength changes of the PhCR and the control microring resonator after each step of the DNA sensing experiment. The resonance shifts of the PhCR after (a) 3-APTES, (b) SPDP linker, (c) 100μM probe DNA and (d) 500nM target DNA are (a) 0.32nm, (b) 0.22nm, (c) 0.79nm and (d) 0.16nm, respectively. The resonance shifts of the control microring are (a) 0.1nm, (b) 0.1nm, (c) 0.27nm and (d) 0.08nm, respectively. These results show that the PhCR has a more than 2-fold enhancement in surface sensing sensitivity compared to the control microring for every step of the DNA sensing experiment. The magnitude of this performance enhancement is consistent with the bulk index sensitivity results reported in the previous section.

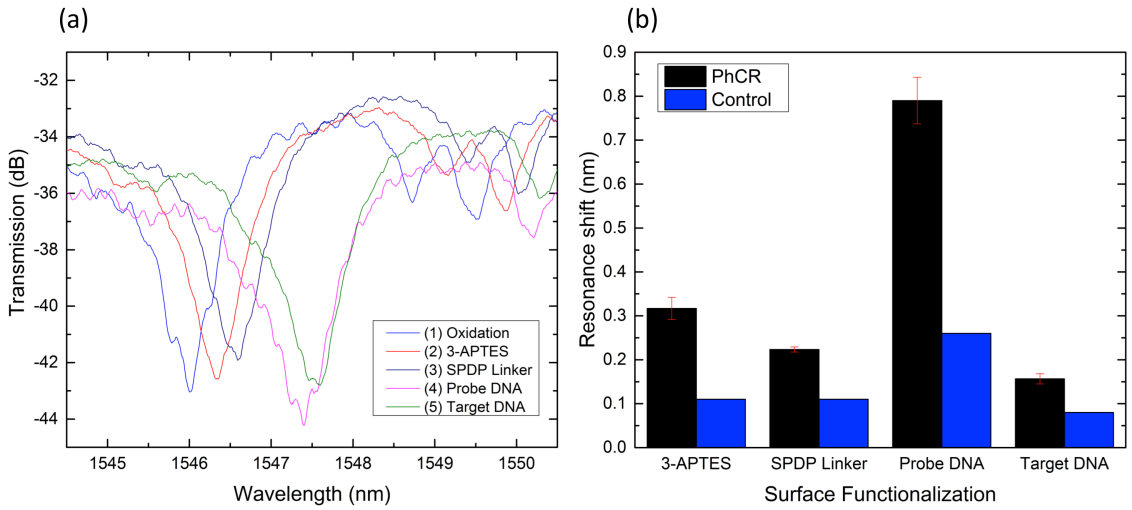

Fig. 3.4. (a) Measured TE-polarized transmission spectra of a PhCR after various surface functionalization steps and after exposure to 500nM target DNA. (b) Resonance red shifts for PhCR and control microring resonators for each step of the DNA detection experiment. Three PhCRs were tested in the experiments.

3.5.3 Label-free biosensing of protein molecules

In addition to the DNA surface sensing experiment, a label-free biosensing experiment with proteins was carried out to further demonstrate the surface sensing capabilities of the PhCR and to verify the previous experimental results. Figure 3.5 (a) shows the measured TE-polarized transmission spectra of the PhCR after each step of the surface functionalization processes and after capture of various concentrations of the target protein, streptavidin. As expected, the resonance red shifts after each step of the process due to the increase in effective refractive index of the PhCR that results from the molecular attachments. Figure 3.5 (b) summarizes the resonance wavelength changes for the PhCR and conventional microring resonator during the protein sensing experiment. The resonance red shifts of the PhCR after (a) 3-APTES, (b) 200μM biotin, (c) 20nM

streptavidin, (d) 120nM streptavidin and (e) 320nM streptavidin are (a) 1.23nm, (b) 0.81nm, (c) 0.18nm, (d) 1.77nm and (e) 2.42nm, respectively. The resonance red shifts of the control microring are (a) 0.58nm, (b) 0.25nm, (c) 0.08nm, (d) 0.75nm and (e) 1.23nm, respectively. The data suggest that most, if not all, biotin probes are hybridized with streptavidin targets at a streptavidin concentration between 120 and 320nM, which is consistent with prior work [70]. Similar to the DNA surface sensing experiment, the protein sensing experiment shows that the PhCR has more than a 2-fold enhancement in detection sensitivity compared to the control microring for every molecular attachment step. Note that a larger resonance shift was experienced after 3-APTES attachment in the protein experiment.

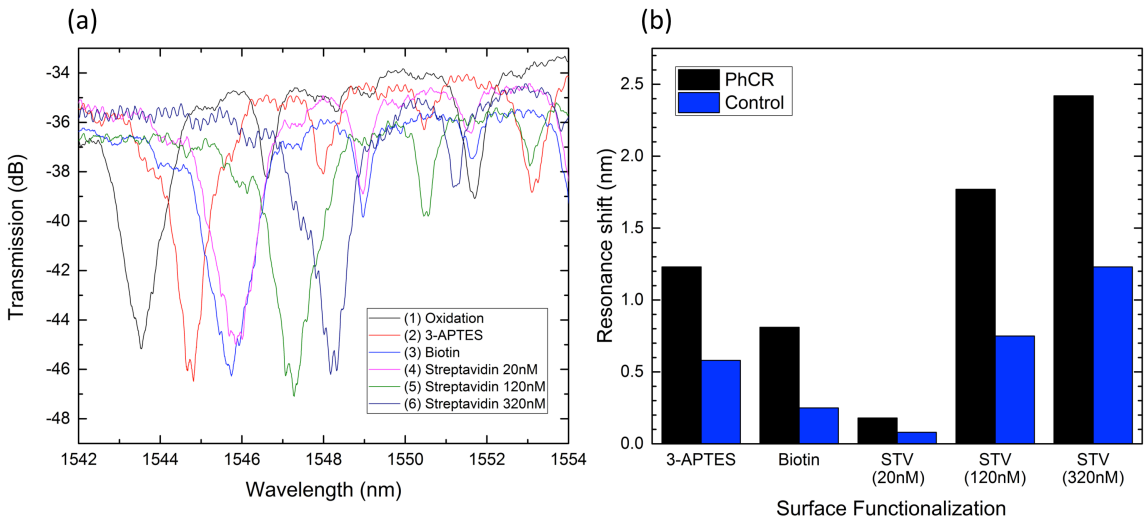

Fig. 3.5. (a) Measured TE-polarized transmission spectra of the PhCR after various surface functionalization steps and after exposure to various concentrations of target proteins. (b) Resonance red shifts for PhCR and control microring resonators for each step of the protein detection experiment. STV: streptavidin.

Based on prior work [70], it is expected that an incomplete monolayer of 3-APTES was formed in the DNA sensing experiments; however, the same relative coverage was likely formed on both the PhCR and the control microring such that a fair comparison of sensing performance took place. It is also possible that slightly more than a single layer of 3-APTES molecules was attached in the protein experiments but, again, the same conditions were applied to the PhCR and control microring ensuring the integrity of the sensing comparison. Given that the additional air holes present in the PhCRs led to an increase of only ~32% in total accessible surface area for molecular attachment (i.e., at the Si-air interfaces) compared to the control microring, the 2-fold detection sensitivity enhancement in both bulk sensing and surface sensing experiments indicates that the optical mode profile, and more specifically the evanescent field in the photonic crystal air holes, plays a significant role in the measured sensitivity enhancement. We note that the similar enhancement for bulk and surface sensing is consistent with the field distribution shown in Fig. 3.2 (b), which shows that the field enhancement in the air holes occurs near the Si-air-interface; hence, no additional sensitivity enhancement is experienced by analyte that fills the holes compared to analyte that only binds on the surface of the holes. The experimental results reported here are based on a PhCR with resonances near the dielectric band edge; it is expected that an even higher sensitivity may be obtained if a resonance near the air band edge is used [67,71].

3.6 Conclusions

The detection sensitivity of PhCR-based biosensors due to bulk refractive index changes and specific DNA and protein binding was investigated. The bulk refractive index change detection sensitivity of PhCRs is ~248nm/RIU, which is more than 2-fold greater than that of conventional microring devices. Label-free biosensing of DNA and protein at the nanomolar scale also revealed that PhCRs have a more than 2-fold surface sensing detection enhancement over conventional microring devices. The detection sensitivity enhancement is attributed to the increased light-matter interaction area where the guided mode of the PhCRs interacts with target analyte. With the advantages of high sensitivity, CMOS compatibility and efficient coupling to existing silicon photonics platforms, PhCRs are promising candidates as optical biosensors in future on-chip diagnostic devices.

4. Bloch mode selection in photonic crystal microring resonators

In this chapter, a novel method to select a subset of Bloch modes in silicon-based photonic crystal microring resonators (PhCR) is demonstrated. Bloch modes in the PhCR are calculated and their intensity beating patterns are analyzed. Based on the different spatial intensity distribution for each resonance, a subset of resonances is out-coupled using an output coupler waveguide (CWG) which is positioned at an angle $\theta=90°$ with respect to the input CWG. As shown in theory and experiment, resonances with an even mode number are selected while resonances with an odd mode number are rejected. The highest contrast between mode selection and mode rejection is ~9dB in experiments. This approach opens another design freedom for ring resonator based devices and could potentially reduce the footprint of microring resonator-based multiplexers and add-drop filters.

4.1 Background

Over the past decade, silicon-based optical microring resonators have drawn a great deal of interest for applications in optical signal processing, label-free biosensing, optical interconnects and telecommunications [72]. Compared to conventional photonic structures such as arrayed waveguide gratings (AWG) and Mach-Zehnder interferometers (MZI), optical components based on microring resonators have the advantages of higher integration density and lower power consumption. In optical signal processing, microring resonators have been demonstrated to enable numerous on-chip functionalities such as optical add-drop filters [73,74], electro-optic modulators [75,76], optical delay lines [77], optical logic gates [78,79], and optical routers [80]. These functionalities are especially critical for integrated silicon-based optoelectronic devices in wavelength division multiplexing (WDM) systems. One path forward to further improve the performance of microring resonators is to incorporate design modifications that impart new functionalities. For example, the photonic crystal microring resonator (PhCR) [60,71,81-82], which utilizes a one-dimensional photonic crystal (PhC) waveguide instead of a conventional silicon waveguide, functions as a standard microring resonator but with a smaller footprint and a highly dispersive characteristic. Thus, the PhCR platform has the potential to realize compact device integration as well as improved performance metrics in optical signal processing and on-chip chemical/biological sensing. While the microscopic optical mode profile near the sidewalls of the PhCR has been shown to be favorable for increasing the detection sensitivity of microrings in label-free bio-sensing experiments [81], the potential advantages of the macroscopic optical mode profile (i.e., Bloch modes) of the PhCR for optical signal processing have yet to be explored.

The periodic structure of the PhCR leads to a strong slow-light dispersion near the Brillouin zone edge and introduces Bloch modes [60,71], yielding intensity beating mode patterns [83,84] in the resonator. Due to the substantially different spatial intensity distributions for each resonance, it should be possible to preferentially select a subset of resonances by strategic placement of output coupling waveguides (CWG) along the microring. Such a wavelength selection method would provide more design freedom to on-chip optical interconnects and potentially reduce the footprint of microring resonator-based multiplexers and add-drop filters.

In this chapter, the design and fabrication of the PhCR are first discussed and the optical properties are explained. Next, Bloch modes in the PhCR are identified using three-dimensional finite difference time domain (FDTD) calculations. Then, resonant mode distributions in the PhCR are analyzed by the fast Fourier transform (FFT) method. Finally, by utilizing spatial beating mode patterns in the PhCR with appropriately positioned output CWGs, output transmission spectra are calculated and measured, which result in the demonstration of Bloch mode selection in the PhCR.

4.2 Device structure and transmission spectra

Figure 4.1(a) shows a top-view scanning electron microscope (SEM) image of a fabricated PhCR coupled with a single curved input CWG. The bending radius of the input CWG (~7.16μm) is the same as that of the PhCR. The input CWG is coupled at polar angle θ=0°. The device was fabricated by a single step of electron beam lithography (EBL) followed by reactive-ion-etching (RIE) on a silicon-on-insulator wafer with a 3-μm buried oxide layer and a 220nm silicon device layer. The silicon device layer was etched through to the buried oxide layer. After etching, the remaining photoresist on top was removed by oxygen plasma. Figure 4.1(b) shows a magnified SEM image of the PhCR at the coupling region. For the design of the PhCR, there are **N**=100 periodic circular holes. The periodicity of the air holes is **a**=450nm with an air hole radius of **r**=0.3**a**, the width of the ring (**d**) is 1.0**a** and the evanescent gap separation (**g**) is 0.4**a**. In order to obtain optimal phase matching between CWGs and PhCRs, the widths of the CWGs (**w**) are designed as 0.75**a**, 0.8**a** and 0.85**a** [60].

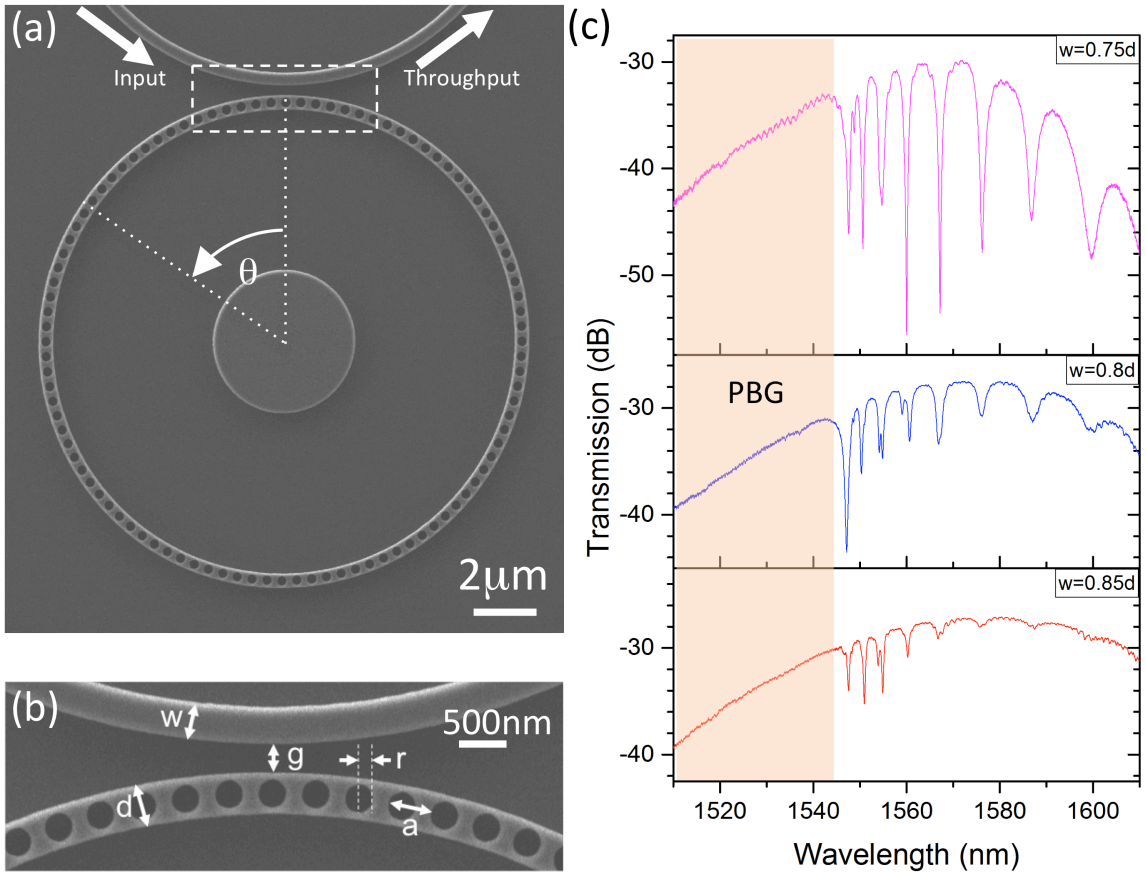

Fig. 4.1. (a) Top-view SEM image of a waveguide-coupled PhCR with 100 periodic circular holes. (b) Magnified SEM image of the PhCR at the evanescent coupling region. (c) Measured TE-polarized transmission spectra of PhCRs with w=0.75d, w=0.8d and w=0.85d.

Transmission spectra were measured using a wavelength scanning technique with an external-cavity tunable laser (Santec TSL-510, 1510 – 1630nm). The output transmission intensities from the devices under test were measured by a photodetector and recorded by a computer. Figure 4.1(c) shows the measured transverse-electric (TE) (electric field parallel to the device plane) polarized transmission spectra of PhCRs with input CWG designs of **w**=0.75**d**, **w**=0.8**d** and **w**=0.85**d**. The spectra show that the band edge of the photonic band gap (PBG) is located near 1545nm as no resonances appear at shorter wavelengths. Due to the slow-light effect, the free spectral range (FSR) between

resonances is highly non-uniform and becomes smaller as the wavelength approaches the band-edge. The maximum calculated group index is ~17. For PhCRs with input CWG widths of 0.75**d** and 0.8**d**, the resonance mode closest to the PBG has an extinction ratio (ER) of ~13dB. The PhCR with input coupling design of **w**=0.75**d** provides the best broad-band phase matching, achieving >10dB ER for resonances across a wavelength range >50nm. The maximum loaded Q-factor of the PhCR is ~2,700, which is limited by fabrication imperfections.

4.3 Simulation results

Given the design of the PhCRs and the slow light phenomenon demonstrated in the transmission measurements, we expect that each transmission resonance should correspond to a distinct and periodic mode pattern, similar to that which has been reported in prior work. In order to elucidate the optical properties of each resonance, 3-D FDTD simulations were carried out [36]. The design parameters of the PhCR used in the simulations were extracted from the SEM images of fabricated devices in order to ensure close comparison between experimental and simulation results. The slight difference in resonance wavelengths between the experimental and simulation results (~10nm blue-shifted in simulation) is likely due to slight errors in the dimensions estimated from the SEM images and inaccuracies arising from the mesh discretization in the simulation.

4.3.1 Transmission spectrum and optical mode profiles

Figure 4.2 (a) shows the calculated TE-polarized throughput-port transmission spectrum normalized to the input intensity. From the transmission spectrum, the maximum group index is calculated to be ~65 and the maximum loaded Q-factor is ~6,700. The calculated group index is higher in simulation than in experiment due to the slight difference in effective index in simulation and experiment, as the effective index determines the resonance wavelengths, which in turn determine the FSR, which is used to calculate the group index. We note that the reported loaded Q-factor is likely limited by the simulation time utilized in this work (24,000 ps), as the calculated intrinsic Q-factor of the PhCR is $\sim 2\times10^{5}$.

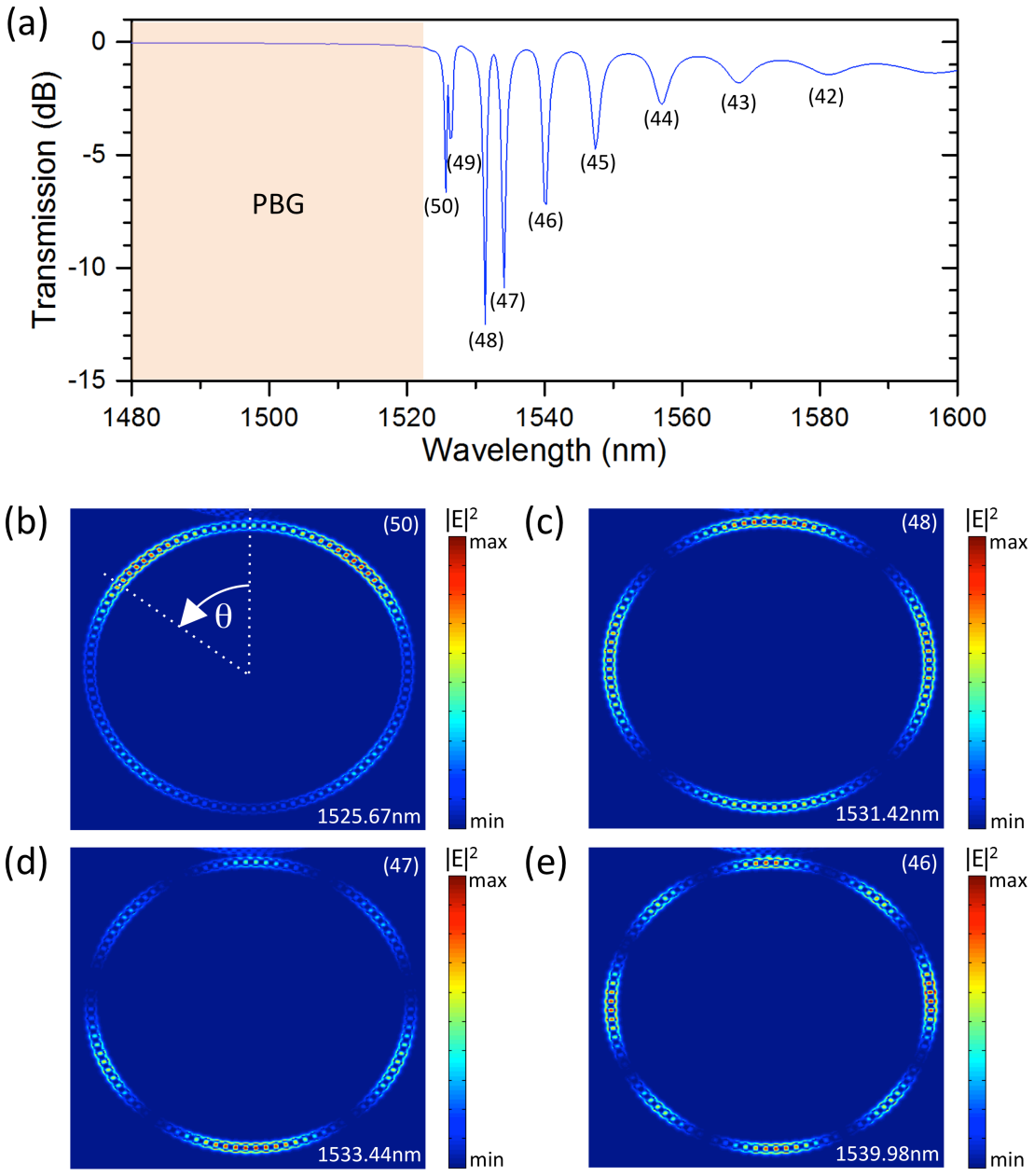

Fig. 4.2. 3-D FDTD calculated TE-polarized (a) throughput spectrum of the PhCR. Resonance dips are labeled by their mode numbers (m). (b-e) intensity ($|E|^2$) mode profiles at resonance wavelengths of 1525.67nm (m=50), 1531.42nm (m=48), 1533.44nm (m=47) and 1539.98nm (m=46). The period of intensity modulation increases with the resonance wavelength.

Figures 4.2(b)-(e) show the calculated TE-polarized intensity ($|E|^2$) mode profiles in the silicon band of the PhCR. The mode profiles show a strong periodic intensity

modulation for each resonance. The number of modulation periods is always an even number and increases linearly as the resonance wavelength increases. For each intensity mode profile, the modulation pattern is oriented with the beating antinode aligned to the position of the input CWG (θ=0°).

4.3.2 Spatial Fourier transforms

In order to further analyze the intensity modulation patterns of the PhCR, the spatial patterns (real space) are mapped to the propagation constant distribution (k-space) using the spatial Fourier transform method [85].

Figure 4.3(a) shows the calculated intensity ($|E|^2$) profiles of the resonances taken at the center of the PhC waveguide. The node(s) (minimum intensity) and antinode(s) (maximum intensity) of each resonance shown in the intensity profiles are due to the beating between the Bloch modes in the PhCR. The strong cross-coupling between the counter-propagation waves can be attributed to three primary sources in the PhCR structure: (1) reflection from the periodic interfaces, (2) backscattering from the interface roughness and (3) backward coupling from the coupling region between the PhCR and the input CWG.

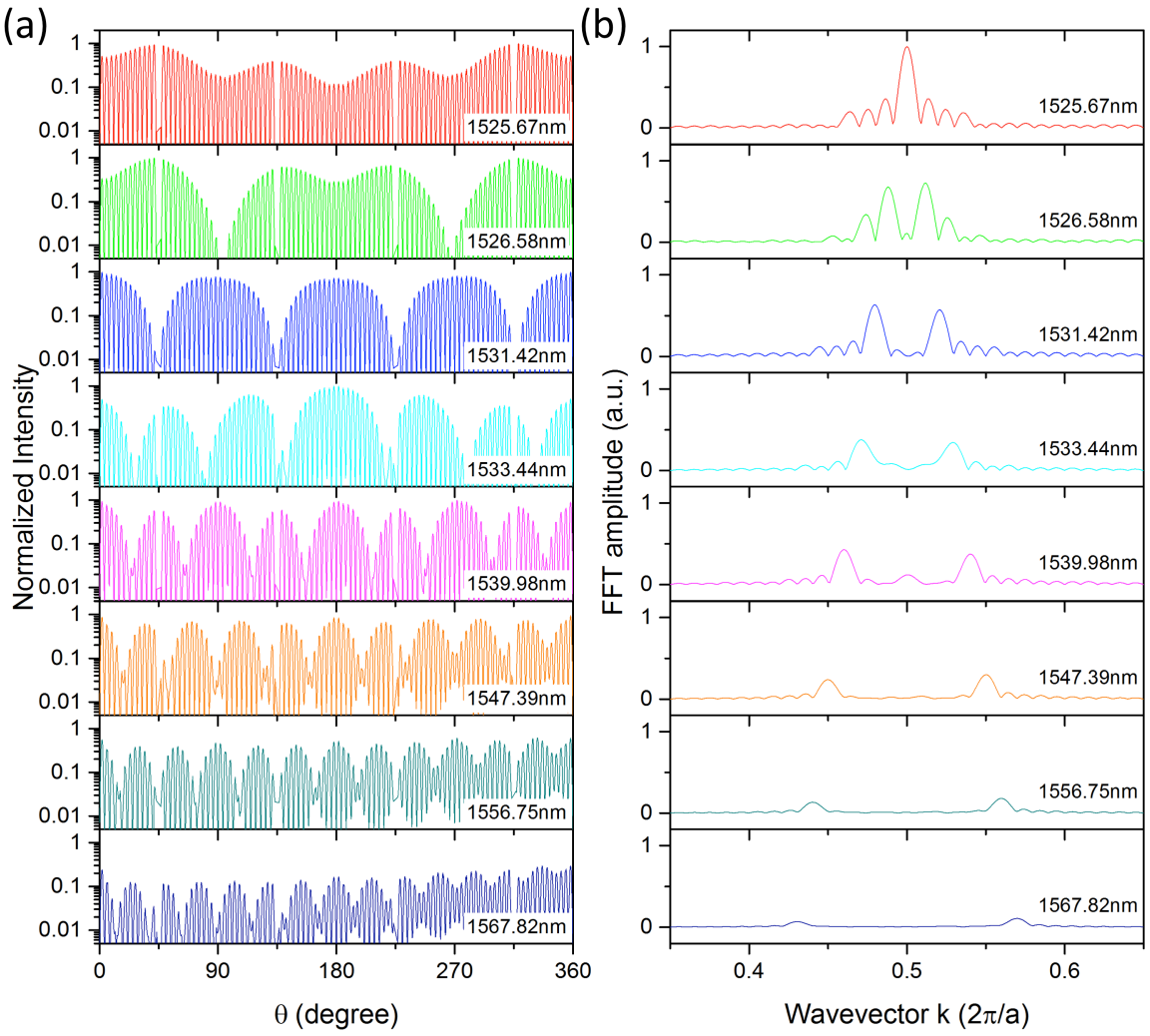

Fig. 4.3. Calculated (a) intensity ($|E|^2$) profiles and (b) Fourier transform amplitudes of the H_z components at the center of the PhC waveguide for the first eight resonances in the PhCR. FFT amplitudes of each resonance are normalized to the maximum value of the FFT amplitude at 1525.67nm.

Figure 4.3(b) shows the Fourier transform of the H_z field profile for first five resonances in the PhCR. The Fourier transform peaks represent the corresponding Bloch mode $\boldsymbol{k}$ components. Except for the first resonance, all other Fourier transform spectra show two $\boldsymbol{k}$ components in the first Brillouin zone: $\boldsymbol{k_1 = m(2p/Na)}$ is the forward propagating component and $\boldsymbol{k_2 = K - k_1}$ is the backward propagating component, where

$\boldsymbol{m}$ is the mode number of the Bloch modes ($|\boldsymbol{m}| \leq \boldsymbol{N/2}$) and $\boldsymbol{K} = \boldsymbol{2p/a}$ is the reciprocal space lattice vector. In addition, the number of beating node(s) can be expressed as $\boldsymbol{B} = \boldsymbol{(a/2p)|k_1-k_2|} = \boldsymbol{N - 2m}$. As shown in Fig. 4.3(a), one beating antinode is always located at θ=180° as $\boldsymbol{B}$ is an even number. Another beating antinode is located at θ=90° when $\boldsymbol{B}$ is a multiple of four. Based on the intensity profiles along the ring as shown in Fig. 4.3(a), one can expect that an output CWG placed at θ=90° will only select the even (m) resonances while an output CWG at θ=180° could select all the resonances. Moreover, if an output CWG is placed at θ=60° or at θ=120°, it would only select resonances with m equal to multiples of three (e.g., m=3 or m=6).

4.4 Device design for Bloch mode selection

Inspired by the Bloch mode profiles, additional simulations were carried out for PhCRs with output CWGs located at polar angles of θ=90° and θ=180° with respect to the input CWG, as schematically illustrated in Fig. 4.4.

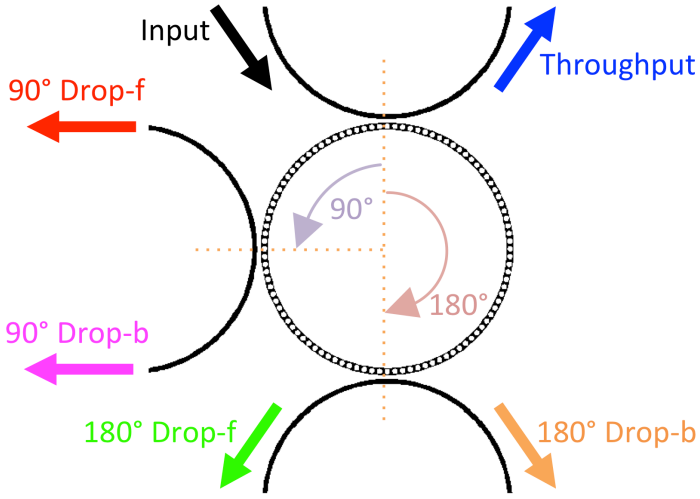

Fig. 4.4. Schematic of PhCR with two output CWGs that are positioned at polar angles of θ=90° and θ=180° with respect to the input CWG.

Figure 4.5 shows the 3-D FDTD calculated TE-polarized throughput transmission spectrum, as well as the drop-port in forward propagation (Drop-f) and drop-port in backward propagation (Drop-b) transmission spectra in the output CWGs at θ=90° and θ=180°. In the Drop-f-port and Drop-b-port spectra, the CWG at θ=90° preferentially selects a subset of resonance modes – all even ***m*** resonances (beating antinode at θ=90°) are selected – while all odd ***m*** resonances (beating node at θ=90°) are rejected. All resonances are selected when output CWG is place at θ=180°, as there is always a beating antinode at θ=180°. The average ratio between the output transmission of odd ***m*** resonances at θ=180° and rejected odd ***m*** resonances at θ=90° is ~15.8dB in forward

propagation and ~17.2dB in backward propagation. The transmission ratio is slightly reduced in the forward propagation direction because it is possible for a small portion of the forward propagating signal from the input CWG to couple to the output CWGs even when a resonance condition is not satisfied.

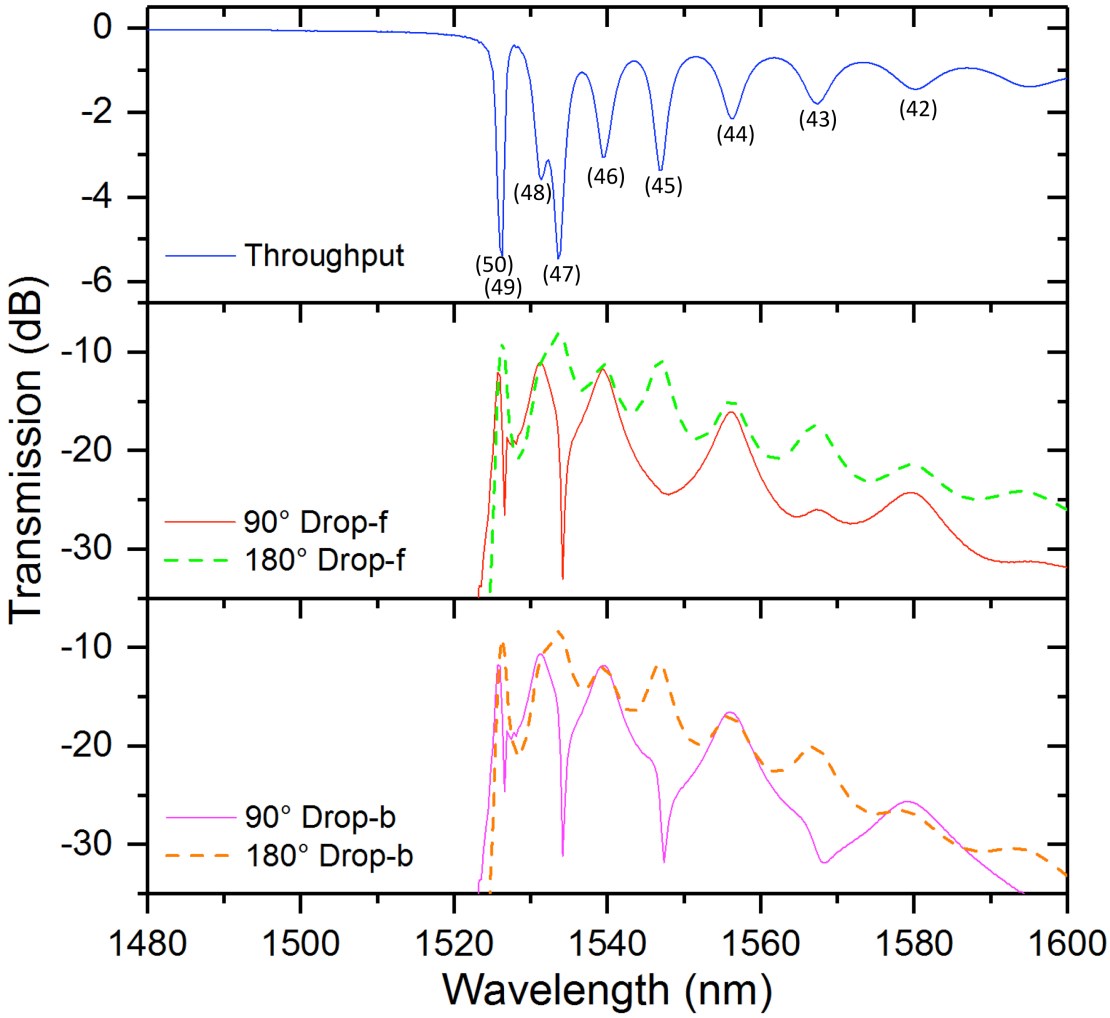

Fig. 4.5. 3-D FDTD calculated TE-polarized (top) throughput spectrum and drop-port spectra in (middle) the forward/Drop-f and (bottom) the backward/Drop-b propagation direction with polar angles of θ=90° and θ=180°.

4.5 Experimental results and discussion

Figure 4.6 shows the top-view SEM of a fabricated PhCR with two output CWGs that are located at polar angles of θ=90° and θ=180° with respect to the input CWG. The design parameters of the PhCR structure are the same as the aforementioned device shown in Fig. 4.1, except for the widths of the CWGs. The widths of the input and output CWGs are set to 0.85**a** instead of 0.75**a** in the previous device. Choosing the narrower CWGs would allow stronger coupling between the PhCR and CWGs, leading to extra optical signal coupling to the drop ports regardless of the resonance conditions and therefore reduced contrast between mode selection and mode rejection in the device.

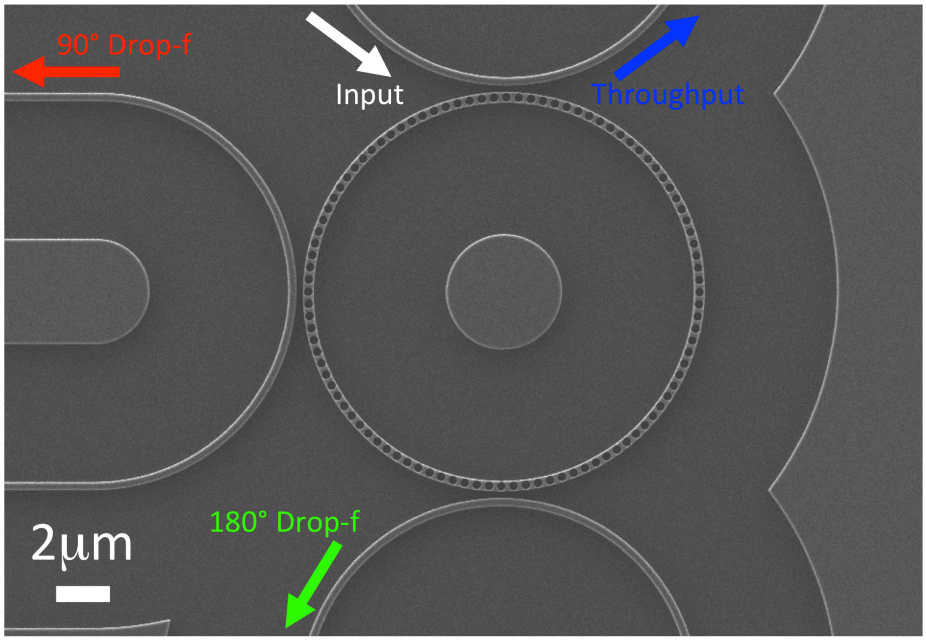

Fig. 4.6. Top-view SEM image of the fabricated PhCR with two output CWGs located at polar angles of θ=90° and θ=180° with respect to the input CWG.

Figure 4.7 shows the measured TE-polarized transmission spectra of the throughput port and Drop-f ports with output CWGs at θ=90° and θ=180°. The measured maximum group index is ~12 with a maximum loaded Q-factor of ~1,500. The reduced Q-factor compared to the device in Fig. 4.1 is mainly due to the addition of the two output CWGs, as they reduce the photon lifetime in the resonator by providing additional out-coupling channels. Note that the band edge of the fabricated PhCR with two output CWGs is ~30nm blue-shifted from the device reported in Fig. 4.1 due to the modified design and slight changes in the fabrication conditions that often arise in separate fabrication runs.

Similar to the simulation results in Fig. 4.5, the Drop-f port at θ=90° is selective to even ***m*** resonances while rejecting odd ***m*** resonances, and all resonances are selected in the Drop-f port at θ=180°. The highest ratio between the output transmission of odd resonances at θ=180° and θ=90° is ~9dB at ~1527nm. The ratio is ~6dB for backward propagation waves out-coupled at Drop-b ports. The transmission ratio between the two output CWGs is reduced in experiment due to a small amount of leakage of the odd modes to the θ=90° Drop-f port, as the large curvature of output CWG could tap out power outside the beating node. We note that the first resonance mode above the PBG in this device has higher transmission in the Drop-f port at θ=180° than in θ=90°, which suggests that it is an odd mode, unlike the simulation results. This discrepancy could due to (1) under-coupling of the ***m***=50 resonance mode due to the wider CWGs in experiment and (2) the ***m***=50 and ***m***=49 resonance modes being overlapped and leading to a superposition of the two modes in the drop port transmission.

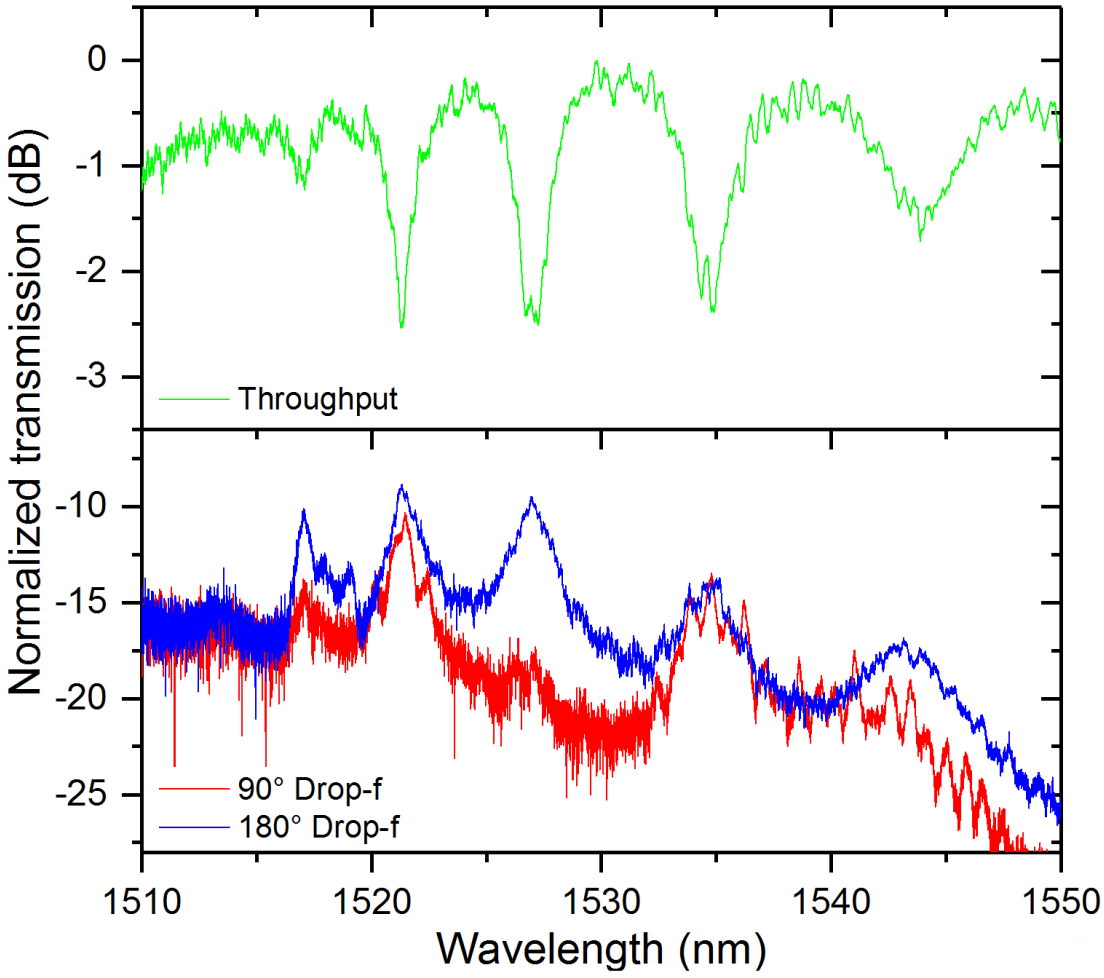

Fig. 4.7. Measured TE-polarized transmission spectra of the PhCR: throughput port (green curve), drop port in forward propagation direction at θ=90° (red curve) and drop port in forward propagation direction at θ=180° (blue curve).

4.6 Conclusions

In conclusion, a novel method of Bloch mode selection based on a silicon photonic crystal microring resonator has been demonstrated. By placing the output coupling waveguide at the beating antinode at an angle $\theta=90°$ with respect to the input coupling waveguide, resonances with an even mode number are selected while resonances with an odd mode number are rejected. The highest contrast between mode selection and mode rejection is ~9dB in experiment. This concept can be extended to enable further refinement in the mode selection by designing output coupling waveguides at other positions, enabling additional design freedom in microring-based multiplexers and add-drop filters.

5. Chirped photonic crystal mode converters for broad-band coupling with highly dispersive photonic crystal microring resonators

In this chapter, evanescent coupling between a photonic crystal (PhC) waveguide and a PhC embedded microring resonator has been demonstrated on the silicon-on-insulator platform. The mode converter comprises 6 linearly chirped air holes that adiabatically couple the light between the silicon waveguide mode and the PhC mode. Three-dimensional finite-difference time-domain simulations reveal a coupling bandwidth of >100nm. From our experiment, the optical spectra show a photonic bandgap located below ~1590nm. At the resonances in the slow-light regime, a loaded quality factor as high as ~2500 was measured and a group index of ~16 in the PhC embedded microring resonator was estimated from the non-uniform free spectral ranges.

5.1 Background

Periodic structures exhibit strong dispersion, enabling dense photonic device integration, which is required for complex on-chip optical circuits. In recent years, several on-chip photonic devices such as tunable reflectors [86], wavelength selective couplers [87], multiplexers [88] and microlasers [89,90] have been demonstrated with periodically patterned waveguides and resonators. Previously, a novel microring resonator structure patterned with periodic circular air holes was demonstrated on a silicon-on-insulator (SOI) platform [60]. By taking advantage of the slow-light effect near the Brillouin zone edge, the footprint of the microring resonator can be reduced while preserving its capacity to support multiple optical channels in wavelength-division multiplexing

(WDM) technology. This structure may also find useful applications in chemical and biological sensing [32], as part of the optical field is located inside the lower refractive index region (i.e., in air holes) that is accessible for molecular attachment.

As the device is operated in the slow-light regime, input-/output-coupling from/to the outside network could be challenging due to the phase mismatch. In our previous work, we achieved phase matching by reducing the width of the silicon waveguide [60]. However, this approach has several disadvantages on device performance. First, the coupling between the silicon channel waveguide and the PhC waveguide has a narrow bandwidth due to different dispersion characteristics. Only a few resonance modes in the resonators can be critically coupled with a specific coupling waveguide width. Second, when the air hole filling factor in the PhC waveguide increases, the silicon coupling waveguide width has to be decreased. Typically this decrease in waveguide width will result in large optical propagation loss when the width is narrower than 300nm [91]. Consequently, the approach of reducing the coupling waveguide width is not suitable for applications requiring broad bandwidth and a large air hole fill factor, such as chemical and biological sensing. In this paper, in order to improve the coupling bandwidth and provide better control on the coupling between the waveguide and the resonator, we design and fabricate a PhC coupling waveguide with chirped PhC mode converters attached at both ends.

This section is organized as follows: In section 5.2 the device design and principle, in this case a PhC embedded microring resonator will be presented. The principle of adiabatic coupling by using chirped PhC mode converters will also be discussed. In section 5.3 the simulation results on chirped PhC mode converters will be presented.

These include results of dispersion characteristics and transmission spectra. In section 5.4 the experimental results will be presented and discussed. These include the transmission spectra and out-of-plane near-field scattering images. This chapter will be conclued in section 5.5.

5.2 Device design and principle

In a conventional microring resonator that has been formed by a dielectric waveguide, the frequency-wavevector dispersion relation in the telecommunication wavelength range is almost linear. Therefore the group index and the free spectral range (FSR) are nearly constant in this range. As a result, the resonance dips in the transmission spectrum are evenly spaced.

However, the situation is different when a highly dispersive structure is used to form a micro-resonator. Inspired by the one-dimensional PhC waveguide, we patterned microring resonators with periodic air holes. The photonic crystal structure enables a strong dispersion characteristic near the photonic bandgap (PBG). When the wavelength of light approaches the photonic band edge, the group index increases as the group velocity is close to zero. As the FSR is inversely proportional to the group index, the resonant dips are not evenly spaced in the transmission spectrum and the FSR becomes minimum when wavelength of light is near the band edge [60].

By introducing the slow-light dispersion into the microring resonator, the PhC embedded microring resonator can have the same FSR as a larger size conventional microring resonator. Hence we can reduce the required footprint of the micro-resonator,

especially in some applications where FSR is a major consideration, such as the WDM system.

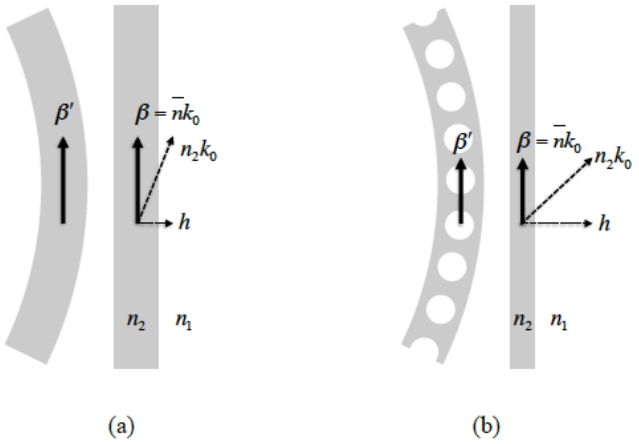

Fig. 5.1. Schematic of the coupling wavevectors between the input waveguide and (a) the standard ring resonator and (b) the one-dimensional PhC microring resonator. β is the propagation wavevector in the waveguide. β' is the propagation wavevector of light traveling in the ring.

In general, we control the coupling strength by matching the phase velocity between the waveguide mode and the resonance mode to couple the light into/out from the microresonator from/to the outside network. When we consider the standard waveguide-coupled ring resonators as shown in Fig. 5.1 (a), the phase matching condition is achieved (β = β') when the width of the waveguide is the same as that in the ring (we assume the effect of the bending of the ring is minimal). In addition, the coupling bandwidth is wide because both the waveguide and the ring have identical dispersion properties.

However, the phase matching is more complicated when we consider the coupling between a linear dispersive waveguide and the highly dispersive one-dimensional PhC microring resonator as shown in Fig. 5.1(b). As we introduce periodic air holes with lower refractive index along the ring, the effective index (as the propagation wavevector,

β') of the ring is significantly reduced. In order to match the phase velocity between the ring and the input waveguide, we can reduce the width of the waveguide such that its propagation wavevector β is equal to β' [60]; however, the aforementioned drawbacks of reduced bandwidth and limited air hole fill factor result.

In order to enhance the coupling bandwidth and have more freedom in controlling the coupling, here we propose and demonstrate an adiabatic coupling approach by using a chirped PhC mode converter. Figure 5.2 shows the schematic of the chirped PhC mode converter for coupling between the silicon waveguide and one-dimensional PhC microring resonator. The mode converter converts the light from the waveguide propagation mode to the PhC propagation mode. It is comprised of several chirped PhC air holes with different radius and lattice constant. By using this design, the coupling bandwidth of the whole system is now controlled by the mode converter. The design parameters of chirped PhC mode converter are based on the dispersion characteristic simulations described in next section.

The design parameters of the one-dimensional PhC microring resonator in this paper are the same as in [60]. The structure is built on the SOI platform with a 250nm thick device layer. The silicon layer is etched through to the buried oxide layer for the waveguides/ring/air holes (i.e., the silicon etch depth is 250nm). There are **N** = 100 circular air holes on the ring resonator, resulting in a ring radius of ~7.16μm. The periodicity of the air holes is **a** = 450nm, the hole radius is **r** = 0.3**a** = 135nm, the width of the ring is **w** = **a** = 450nm.

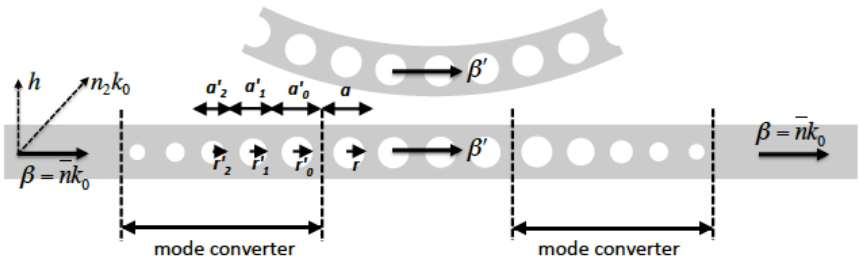

Fig. 5.2. Schematic of the PhC mode converters for coupling between silicon waveguide and one-dimensional PhC microring resonator. The mode converter converts the waveguide wavevector β into PhC wavevector β'.

5.3 Simulation results

In order to obtain the design parameters of the chirped PhC mode converter, we calculated the dispersion characteristics of the one-dimensional PhC waveguide. The simulations were done by MIT Photonic-Band (MPB) software that utilizes the plane-wave expansion (PWE) method [37]. Figure 5.3 (a) shows the calculated contour map of the wavevector k of the chirped PhC waveguide at the band edge frequency ω_o. The polarization is transverse-electric (TE) like (electric field parallel to the device plane). The y-axis represents the normalized lattice constant a' and the x-axis represents the normalized hole radius r'. This frequency ω_o is corresponding to the band edge frequency of the unchirped one-dimensional PhC waveguide to form the microring resonator with design parameters shown in section 5.2. At frequency ω_o, the wavevector of the unchirped PhC waveguide is k_o. The color area in the contour map depicts the possible solutions of the chirped PhC waveguide. The solutions of the chirped PhC have band edge frequency ω larger than ω_o, while wavevector k is also larger than k_o.

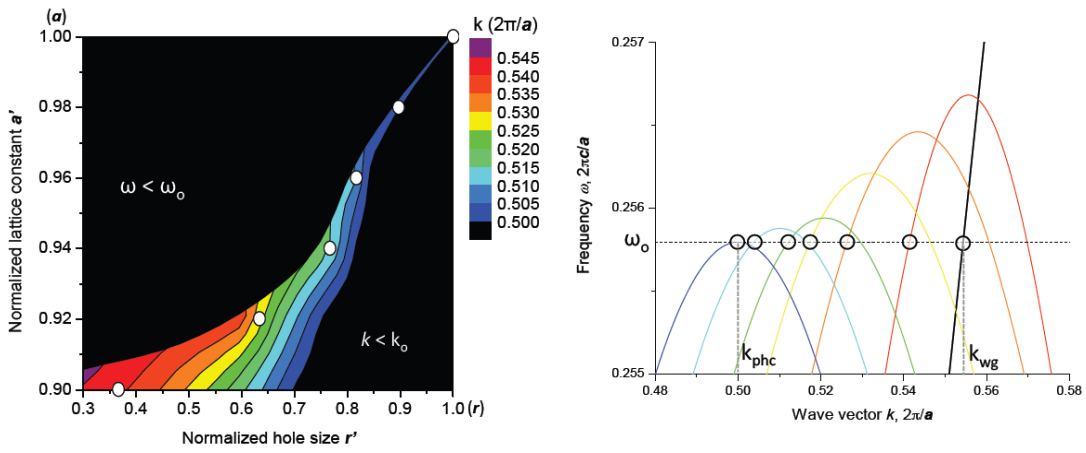

Fig. 5.3. (a) Contour map of wavevector k of the chirped PhC at the band edge frequency. The 6 linear chirped parameters (0.37**r**, 0.90**a**), (0.63**r**, 0.92**a**), (0.77**r**, 0.94**a**), (0.82**r**, 0.96**a**), (0.90**r**, 0.98**a**) and (1.00**r**, 1.00**a**) are circled. ω_o is the band edge frequency of unchirped PhC. k_o is the band edge wavevector of unchirped PhC. (b) Calculated band diagram of the 6 selected chirped PhC parameters and the dielectric waveguide. ω_o is the band edge frequency. k_{phc} is the band edge wavevector in the unchirped photonic crystal waveguide. k_{wg} is the wavevector of the silicon channel waveguide.

In this work, we selected six solutions (including the original unchirped PhC) for the linearly chirped PhC waveguide to form the mode converter. These six linear chirped parameters (r', a') are (0.37r, 0.90a), (0.63r, 0.92a), (0.77r, 0.94a), (0.82r, 0.96a), (0.90r, 0.98a) and (1.00r, 1.00a) and are represented by the circles in the contour map of Figure 3(a). The normalized lattice constants of six holes linearly increase from 0.90a to 1.00a, and corresponding air hole radii were selected to provide evenly spaced projected wavevectors at frequency ω_o. These parameters correspond to a smallest air hole radius of 50 nm, which is within the fabrication limitation of the-state-of-the-art electron beam lithography.

Based on these parameters, we calculated the corresponding dispersion curves of the chirped PhC and the dispersion curve of the dielectric waveguide as shown in Figure

3(b). At the band edge frequency ω_o, the wavevector is coupled from/to k_{phc} of the unchirped photonic crystal waveguide to/from k_{wg} of the dielectric waveguide. In order to understand the coupling efficiency and bandwidth, we simulated the transmission spectra by using the finite-difference time-domain (FDTD) method.

We simulated the transmission spectra using a three-dimensional FDTD method [36]. The design parameters are the same as depicted in Section 2 and Section 3.1. The input polarization is TE-like**.** Figure 5. 4(a) shows the schematic of our structure under the simulation environment. Our structure consists of 11 air holes in the coupling waveguide, where 10 of them are used to form two sets of chirped PhC mode converters. The gap separation between the coupling waveguide and PhC ring is 135nm, which has been selected to provide high extinction ratio of resonance dips.

Figure 5.4 (b) shows the transmission spectrum from this structure and Figure 5.4 (c) shows the transmission spectrum of the control structure with only the coupling waveguide. The spectra show that the photonic band edge is located at ~1690nm. We note that this band edge is ~150nm red-shifted compared to our bandgap simulations reported in [60]. We suspect the deviation could due to differences in the simulation environment such as mesh size and bending of PhC waveguide in the ring.

In Fig. 5.4(b), we observed resonance peaks and resonance dips with non-uniform FSRs in the wavelength range of ~1690nm to 1850nm. They are associated with the PhC microring resonator as the resonance peaks and dips do not appear in the control spectrum. The FSR of resonances is ~22nm at wavelength of ~1830nm and is reduced to ~5.5nm at wavelength of ~1690nm. Thus the group index of PhC mircroring resonator increases from ~3.4 at wavelength of ~1830nm to ~11.6 at wavelength of ~1690nm. The

increase of group index is due to the slow-light effect near the band edge. The highest simulated loaded quality factor is ~1000 at resonance wavelength of ~1695nm. While at resonance wavelength of ~1840nm, the simulated loaded quality factor is only ~110. The enhancement of quality factor close to band edge can be due to (1) better confinement in the PhC microring resonator at shorter wavelength and (2) slow-light effect [6]. At wavelengths close to band edge, resonance peaks appear instead of resonance dips. We suspect this effect is due to the bandgap mismatch between the straight PhC waveguide and bended PhC microring resonator. We suggest that the bandgap matching can be improved by bending the coupling PhC waveguide to the same curvature as the microring.

From the transmission spectrum in Fig. 5.4 (b), the resonance dips have high extinction ratio (>10dB) for wavelengths from ~1730nm to ~1810nm, which indicates a similar coupling condition in this wavelength range. As the quality factor is significantly decreased at longer wavelengths close to 1850nm, the critical coupling condition changes and the extinction ratios of resonance dips decrease. When we take into account the resonance peaks from wavelengths of ~1680nm to ~1730nm, the chirped PhC mode converter provides a coupling bandwidth of >100nm between the silicon waveguide and the PhC ring.

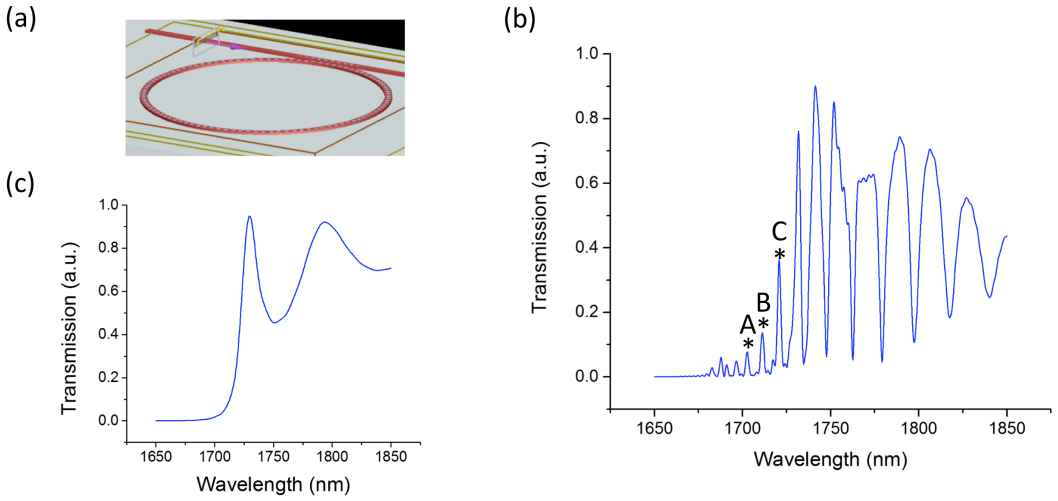

Fig. 5.4. (a) Schematic of chirped PhC mode converters and PhC microring resonator under FDTD simulation environment. (b) 3D FDTD simulated TE-polarized transmission spectrum of chirped PhC mode converters coupled with PhC microring resonator. (c) 3D FDTD simulated TE-polarized transmission spectrum of control structure without the PhC microring resonator.

We labeled the first few slow-light modes as mode A (1703.32nm), mode B (1711.24nm) and mode C (1721.91nm) near the band edge in Fig 5.4 (b), and we simulated their corresponding steady-state intensity profiles as shown in Fig. 5(a)–(c).

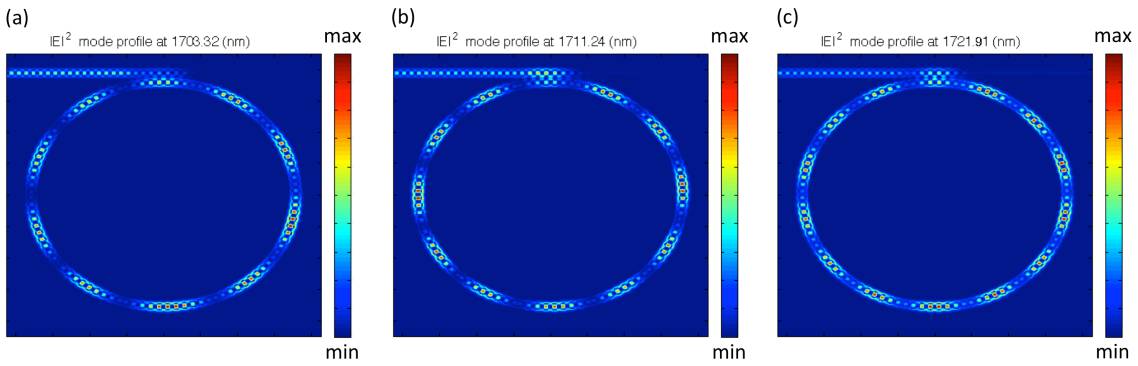

Fig. 5.5. Simulated steady-state intensity profiles of the structure at wavelength of (a) 1703.32nm, (b) 1711.24nm and (c) 1721.91nm. The input beam is launched from top left to top right in each profile.

The intensity profiles confirm that the input beam has been coupled into the PhC ring resonator at resonance peaks/dips. The mode profiles have even number of nodes across the ring, resulted from the beating of forward and backward light in the resonator. When the resonance wavelength decreases, the number of nodes across the ring also decreases. As the mode profiles show 14 nodes at 1721.91nm, 12 nodes at 1711.24nm and 10 nodes at 1703.32nm. These phenomena are in good agreement with our previously calculated results under a different simulation platform [60].

5.4 Experimental results and discussion

Figure 5.6 (a) shows the top-view scanning electronic microscope (SEM) image of our fabricated chirped PhC mode converters with PhC microring resonator. The measured waveguide width is 460nm for both the PhC waveguide in the ring and the waveguide in coupling region. The measured coupling gap separation is 188nm. For the air holes to form the PhC microring resonator, the measured radii are around 150nm. The radius of the microring resonator is around 7.15mm. The strong charging effect under the SEM image suggests that the silicon device layer has been etched down to the buried oxide layer.

Figure 5.6 (b) shows the zoom-in top-view SEM image of the coupling region between the chirped PhC mode converters and PhC microring resonator. The measured air hole radii for the chirped PhC mode converters are 58nm, 96nm, 118nm, 121nm, 134nm and 147nm, respectively. From the measurements, the fabricated air hole radii for the mode converters are ~10-20nm larger than our design values. The coupling gap

separation is ~30nm wider, and the air hole radii on PhC microring resonator are ~15nm larger. From the zoom-in image, we also found that the shape of the air hole is slightly distorted. We believe that such deviations in the hole radii and waveguide width can be attributed to artifacts in the fabrication process, such as the overdose and the proximity effect in the EBL exposure, or the isotropic etching in the RIE process.

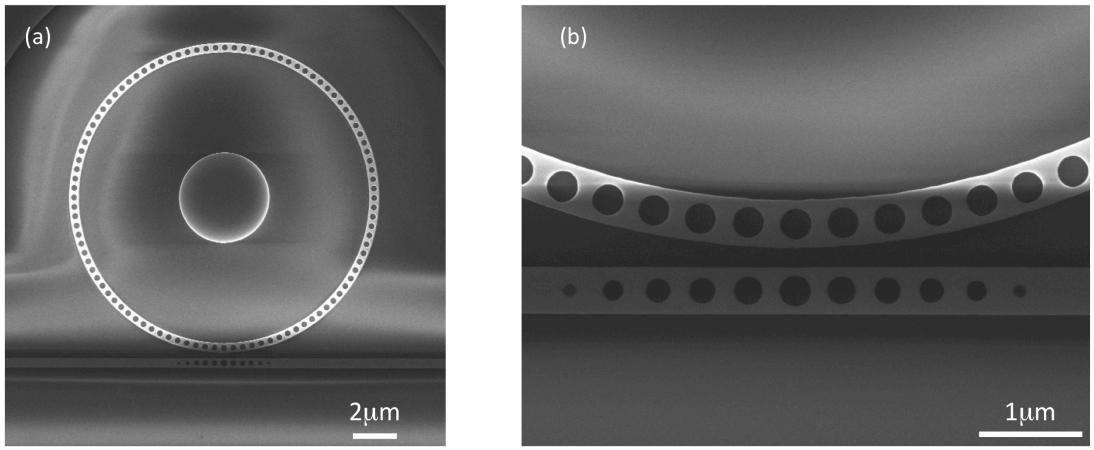

Fig. 5.6. (a) Top-view SEM image of fabricated chirped PhC mode converters with PhC microring resonator. (b) Zoom-in top-view SEM image of the coupling region.

5.4.1 Transmission spectrum

Fig. 5.7(a) shows the measured TE-polarized transmission spectrum of the PhC microring resonator coupled to chirped PhC mode converters shown in Fig. 5.6. The wavelength resolution is 0.1nm. In the spectrum, we observed almost zero transmission from 1510nm to 1590nm. From 1590nm to 1630nm, there are several resonance peaks with high extinction ratio. The FSRs between resonance peaks are non-uniform and range from 8nm at longer wavelength to <4nm at shorter wavelength close to 1590nm. The

non-uniform FSRs suggest the PhC microring resonator introduces the resonance peaks. The experimentally measured spectrum is similar to our calculated one for wavelengths close to and shorter than the band edge. From this result, we deduce the photonic bandgap is located at wavelengths below ~1590nm. The wavelength of the band edge is ~100nm blue-shifted compared to our FDTD simulation results presented in section 5.3. Such blue-shift can be attributed to larger air hole dimensions of the fabricated device.

We also note that the wavelength of the band edge is ~50nm longer than the one in our previous experimental results reported in [60] with same design parameters. Such red-shift of the band edge could be due to the different thickness of the device layers of the two different sets of SOI wafers that were used. Due to the red-shift of the band edge, only a ~40nm of wavelength range outside bandgap can be measured from our setup. This induces the difficulty to compare the coupling bandwidth of the chirped PhC mode converters between experiments and simulations. We suggest a modified design of chirped PhC mode converters and PhC microring resonator could induce the blue-shift of band edge to ~1530nm in future experiment. The new designs have larger air hole size and narrower waveguide width on a SOI substrate with thinner device layer.

We remark that the resonance peaks shown in the spectrum may also result from structures other than the PhC microring resonator such as the mode converters itself. However, the FSRs of resonance peaks do not match with the dimension of any other structures in the design layout to form a Fabry-Perot like response. Moreover, near-field scattering images shown below support this conclusion.

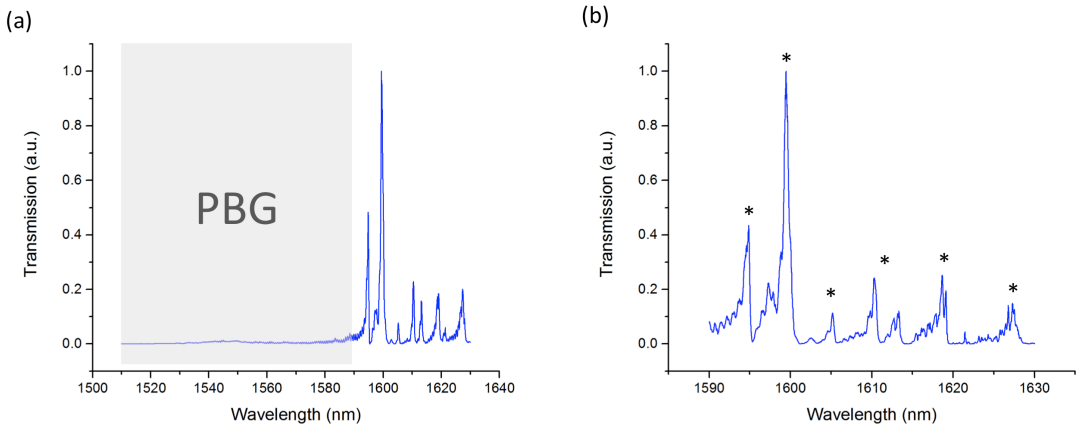

Fig. 5.7. (a) Measured TE-polarized transmission spectrum of the PhC microring resonator coupled by chirped PhC mode converter. PBG: photonic bandgap. (b) Measured TE-polarized transmission spectrum with close-up wavelength range from 1590nm to 1630nm. The resonances are identified with asterisks.

Figure 5.7 (b) shows the measured spectrum in the wavelength range from 1590nm to 1630nm, for wavelengths outside the bandgap region. The wavelength resolution is 0.02nm. We identified the resonances with asterisks in the figure. A loaded quality factor of ~2500 was measured at wavelength of ~1595nm. For wavelengths around 1600nm and 1610nm, we observed doublets for these resonance peaks. The doublets are likely to result from the mode splitting caused by the strong cross coupling between degenerate forward and backward modes in our structure [92].

5.4.2 Out-of-plane infrared image

In order to verify the resonances and photonic bandgap, we performed an experiment to image the out-of-plane near-field scattering. Figure 5.8 (a) shows the near-field image of the PhC microring resonator at wavelength of ~1585nm, where the wavelength is

within the bandgap. Figure 5.8 (b) shows the near-field image at wavelength of ~1614nm, where a resonance peak appears in the spectrum. We observed that there was no scattered light from the PhC microring resonator when the wavelength of light is within bandgap, as shown in Fig. 5.8(a). The scattered spot in the image was from the PhC mode converter region that contributed to the high out-of-plane radiation. When the wavelength is outside the bandgap, there was scattered light from the PhC microring resonator when the wavelength of the input beam matches the wavelength of a resonance peak in the spectrum, as shown in Fig. 5.8(b). Thus these images confirm the existence of the bandgap and that the peaks in the spectrum are from the resonances of the resonator.

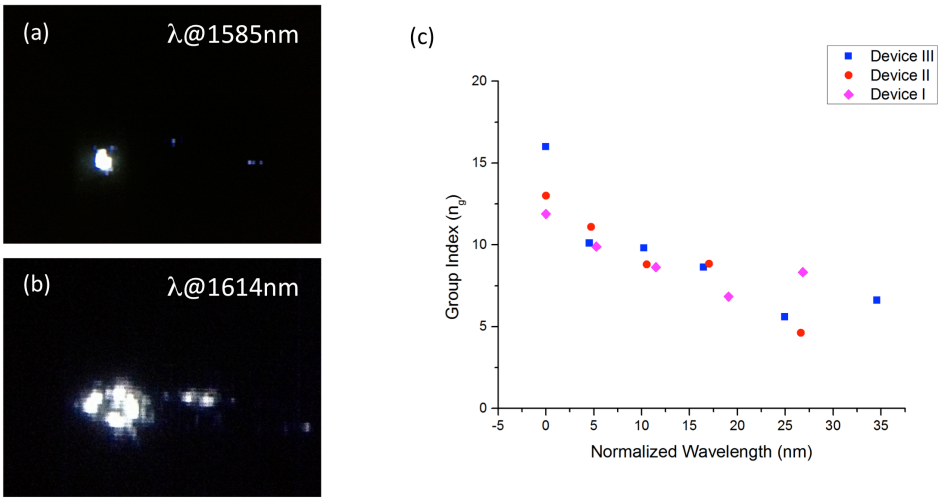

Fig. 5.8. Out-of-plane near-field scattering images of the PhC microring resonator at wavelength of (a) 1585nm (within the photonic bandgap) and (b) 1614nm (outside the photonic bandgap). (c) Group index calculated from the measured spectra.

Figure 5.8 (c) shows the measured group index of PhC microring resonators as a function of normalized wavelength (to the first resonance wavelength near the band edge)

for three different designs with varying coupling gap separations from 160nm to 340nm. We calculated the group index by the non-uniform FSRs from the measured spectra and also the radiated light. The largest estimated group index is ~16. As the group index of a silicon channel waveguide is about 4, we achieved a 4 times enhancement of group index in the PhC microring resonator due to the slow-light effect.

5.5 Conclusions

We propose and experimentally demonstrate evanescent coupling between a silicon waveguide and a PhC microring resonator through chirped PhC mode converters on the SOI platform. Our theoretical studies reveal the chirped PhC mode converter has a broad coupling bandwidth of >100nm. Experimental results show coupling of light from the silicon waveguide to the PhC microring resonator with a photonic band edge located at ~1590nm, a loaded quality factor of 2500 and a group index of ~16 in the slow-light regime. The structure may provide applications in optical signal processing and chemical/biological sensing.

6. Embedded one-dimensional photonic crystal cavity

In chapter 3-5, the applications of photonic crystal microring resonator (PhCR) on label-free biosensing and optical-interconnects are presented. PhCR shows superior performance over conventional platform on bio-sensing, and also demonstrates a novel Bloch modes selection method. These emphasize the importance of optical characteristics such as the light-matter interaction and the field distribution of a photonic structure in numerous applications. While PhCR structure combines the 1-D photonic crystal waveguide with microring resonator, it is also feasible to build a novel nano-photonic device by combing a 1-D photonic crystal nano-beam cavity and a microring structure. This device, name as embedded one-dimensional photonic crystal cavity (EPhCC), shows a surprising high quality factor for a range of graded mirror period over conventional 1-D photonic crystal nano-beam cavity. Moreover, unlike the conventional waveguide butt-coupled cavity, the EPhCC structure can be conveniently implemented in a wavelength-division multiplexing (WDM) system. It is crucial for applications in optical-interconnects such as low-footprint multi-wavelengths low-energy optical modulation.

6.1 Background

In last two decades, one-dimensional (1-D) and two-dimensional (2-D) photonic crystal (PhC) cavities at optical wavelength have been studied extensively due to its excellent compatibility with nano-fabrication process [93-109]. By creating a defect to the periodic dielectric function and minimizing radiation losses, Quality factor of ~10^6 with mode volume of ~$(\lambda/n)^3$ PhC cavities have been recently demonstrated [110]. Compared to 2-D PhC cavities, 1-D PhC cavities offer advantages of reduced footprint, lower mass and simplified geometry. These lead to demonstration of numerous applications including optical-interconnects, sensing, and cavity opto-mechanics. However, most reported 1-D PhC cavities ("nano-beam") were based on waveguide butt couple configurations [110]. An evanescent coupled configuration would be required when employing nano-beam structure into a WDM system. Although the intrinsic quality factor and mode volume of the waveguide butt coupled nano-beam and the evanescent coupled based nano-beam are highly similar, as shown in later sections of this chapter, the coupling waveguide the at the proximity of the nano-beam cavity in evanescent coupling would strongly reduce the photon lifetime in the cavity thus results in a low quality factor cavity. As high quality factor is essential for number of on-chip photonic applications such as cavity opto-mechanics and non-linear optics, better schemes of coupling waveguide designs or nano-beam designs are necessary. In this chapter, we proposed and demonstrated a novel photonic device – embedded one-dimensional photonic crystal cavity (EPhCC). It is similar to and function as a 1-D nano-beam resonator but with superior quality factors and similar mode volumes over a wide range of graded mirror period that one would

usually employed. Moreover, EPhCC structure, unlike conventional nano-beam, provides good compatibility to the WDM system due to its evanescent coupling scheme.

In the following sections, designs, simulation and experimental results of EPhCC structures will be presented and discussed. The comparison between EPhCC and conventional nano-beam structures will also be provided. A shifted-holes scheme to further enhancing the quality factor of EPhCC will be discussed. Continue work for enhancing its optical performance by modifying the coupling waveguide orientation will also be suggested.

6.2 Device structures

There are two types of 1-D PhC cavities will be studied in this paper – (1) conventional waveguide butt coupled nano-beam and (2) the purposed novel EPhCC structure. Schematic diagrams of these structures are depicted in Fig 6.1. All the design parameters that are crucial to optical characteristics of the cavities are identical for both conventional nano-beam and EPhCC. Fig. 6.1(a) shows the top-view schematic of a conventional waveguide butt coupled nano-beam. The nano-beam has a high index region as silicon (index of ~3.5) and a low-index region as air (index of ~1). The nano-beam configuration and key design parameters such as period **a**, air holes filling factors and waveguide width **w** are based on prior work reported in [111]. By minimizing the radiation loss of cavity with quadratic variation of filing factor, this cavity design could provide $>10^7$ intrinsic quality factor. In the schematic in Fig. 6.1(a), there are 30 air holes in the nano-beam, as one graded mirror segment consists of 15 air holes. The waveguide extends from the graded mirror segments to the input and output for butt coupling. This nano-beam structure is the most common configuration due to its convenient coupling scheme and will be used as a control structure in this chapter.

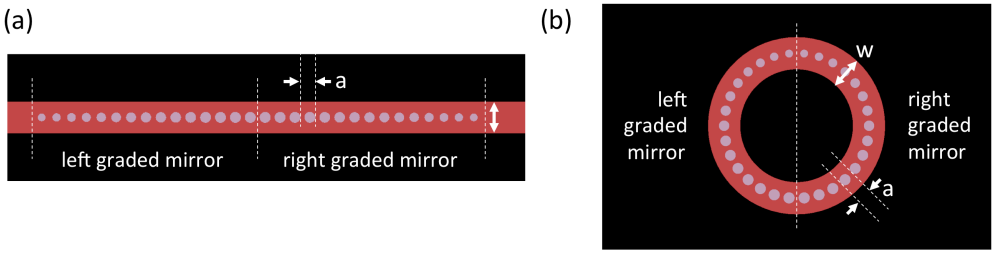

Fig. 6.1. Schematic of (a) the conventional waveguide butt coupled nano-beam, and (b) the embedded one-dimensional photonic crystal cavity. All two schematics have identical design parameters of waveguide width, graded mirror period and air holes filling factor. The area in red color represent high index region (silicon) and the area in grey and black colors represent low index region (air).

Fig. 6.1(b) shows the top-view schematic of an EPhCC. As in Fig. 1(a), the EPhCC has a high index region as silicon (index of ~3.5) and a low-index region as air (index of ~1). One could imagine that the EPhCC is constructed by rolling up a conventional nano-beam to form a ring-shaped nano-beam. Therefore the radius of the ring-shaped EPhCC is equal to the $1/2\pi$ of the total length of the nano-beam. The design parameters of both nano-beam and EPhCC such as waveguide width, graded mirror period and air holes filling factor are identical for fair comparison. In the EPhCC, the distance between last air holes in the left-hand graded mirror and right-hand graded mirror is equal to the period of the PhC structure.

The evanescent coupling nature of EPhCC could potentially provide a better control of coupling strength, thus extinction ratios of resonances, between the coupling waveguide and the EPhCC cavity over conventional butt coupled nano-beam structures. Due to the ring-shaped design, in order to use a coplanar coupling waveguide for evanescent coupling, the coupling waveguide can only be placed near the bottom (south) side of EPhCC in the schematic. Fig. 6.2(a) shows the schematic of coupling waveguide placed at the bottom (south) side of the EPhCC, one can control the width of coupling waveguide and the gap separation between the coupling waveguide and the nano-beam to obtain a desire coupling condition.

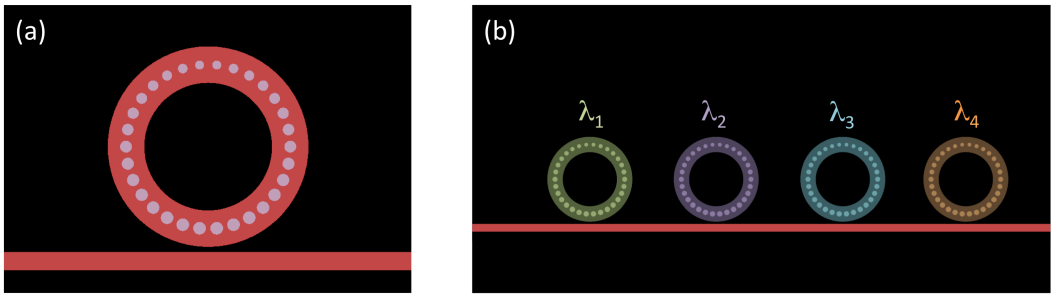

Fig. 6.2. (a) Schematic of the EPhCC with a coplanar coupling waveguide placed at the bottom (south) side of the nano-beam. (b) Schematic for a WDM system that employing a single coupling waveguide evanescently coupled to four EPhCCs with different resonance wavelengths. EPhCC with different colors represent different resonance wavelengths.

By employing evanescent coupled waveguide, EPhCC has advantage of compatibility for WDM system in on-chip optical-interconnects. Furthermore, one can design the resonance wavelength of the nano-beam cavity by slightly modifying the width, filing factors and air holes positions regarding to the center of the ring (in shifted-hole EPhCC design). These modification and wavelength tunings are done without any major compensation on quality factor and mode volume (in the case of shifted-hole design, the quality factor could actually be enhanced). Fig. 6.2(b) shows the schematic diagram for such an example of a WDM system that employing a single coupling waveguide evanescently coupled to four EPhCCs with different resonance wavelengths. Such system has an advantage of much smaller footprint over conventional WDM system that employing multiplexer/de-multiplexer such as arrayed waveguide grating or Mach-Zehnder interferometer. One can also utilize the free-carrier-plasma-dispersion effect in silicon [10] to modulate the resonances of each EPhCC by electro-optic modulation.

6.3 Simulation results

6.3.1 Calculated intrinsic quality factor

In order to elucidate the optical properties such as resonance wavelengths, quality factors, mode volumes, transmission spectra and mode profiles of conventional nano-beam and EPhCC, 3-D finite difference time domain (FDTD) simulation were carried out [36]. In this paper, all the calculations are for transverse-electric (TE) mode (electric field parallel to the device plane). Throughout the simulation, we set **w**=700nm and **a**=330nm as depicted in [111]. The filling factor of air holes are 20% at the center of cavity and 10% at the edge of graded mirror, that result in air hole radii of ~121nm at the center and ~86nm at the edge. These designs parameters are well within the limitation of our fabrication process and potentially could be able to be manufactured by state-of-the-art CMOS fabrication foundry [64].

Fig. 6.3(a) shows the 3-D FDTD calculated quality factors of the fundamental mode with different graded mirror period for conventional waveguide butt coupled nano-beam and EPhCC. In the FDTD simulation, magnetic dipoles were used as optical sources and quality factors were calculated by examining the optical power decay as a function of time. The graded mirror periods used in the simulations were 6, 8, 10, 12, 15, 20 and 25. For both structures, the quality factors increase as the number of graded mirror period increase. As the graded mirror period increase, the reflection coefficient of graded mirror increases, hence enhancing optical confinement and quality factors. At graded mirror period of 20, EPhCC shows more than two times higher in intrinsic quality factor than straight-shaped nano-beam counterparts. As the calculated quality factor of nano-beam is ~$1x10^6$, while the calculated quality factor of EPhCC is ~$2.2x10^6$. Note that the quality

factors calculated here are representing the intrinsic quality factors, a modification of the structure such as adding a coupling waveguide for coupling light in-to/out-of evanescent coupled nano-beam would further decease its loaded quality factors. The calculated mode volume for conventional butt coupled nano-beam and EPhCC are ~0.05 μm^3 or ~0.013 λ^3 (λ is 1.55μm). The mode volumes are relatively irrelevant to the graded mirror period when the period is higher than 12, as most of the fundamental mode field energy are concentrated in the silicon region between the left and right graded mirror segments.

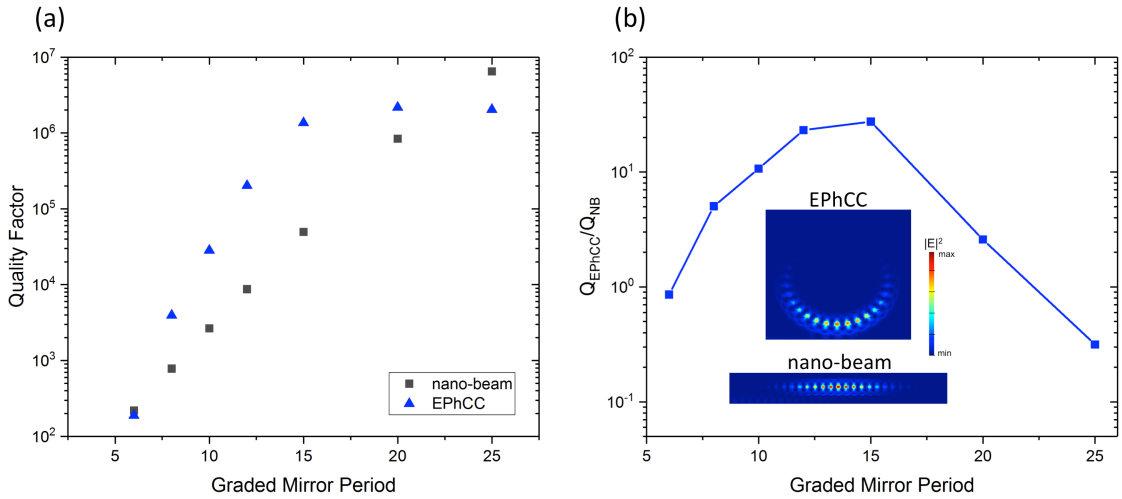

Fig. 6.3. (a) 3-D FDTD calculated quality factors of the fundamental mode with different graded mirror period for butt coupled nano-beam and EPhCC. (b) .The ratio of calculated quality factors of EPhCC and butt coupled nano-beam. (Inset) TE-polarized $|E|^2$ mode profiles of the fundamental mode of conventional nano-beam and EPhCC.

Fig. 6.3(b) shows the ratios of calculated intrinsic quality factors of EPhCC and conventional nano-beam. The EPhCC structure shows a superior intrinsic quality factor over conventional nano-beam for period between 8-20. We contributed the quality factor enhancement is due to the increase of reflection coefficient of ring-shaped graded mirror in the EPhCC structure, as the end of left graded mirror attached to the other end of right

graded mirror that effectively increase the mirror period. The resulted mirror reflectivity enhancement in EPhCC overcomes the additional bending loss due to high-curvature and achieves a highest of ~27 fold improvement over conventional nano-beam at mirror period of 15. Note that the enhancement factor decreases when graded mirror period increases from 15 to 25. This is because the mirror reflectivities are almost unchanged among these designs, but the bending losses of the ring-shaped EPhCC become the major source of optical loss in the cavity. However, in order to maintain a small footprint for dense integration for on-chip optical-interconnects applications, a graded mirror period of <20 would be desirable, in where EPhCC provide significant improvement of quality factor over conventional nano-beam structures.

Inset of Fig. 6.3(b) shows the TE-polarized $|E|^2$ mode profiles of the fundamental mode of conventional nano-beam and EPhCC. For the conventional nano-beam, the optical field is localized between two graded mirror segments and gradually decayed from the center of the nano-beam to the two ends of graded mirrors. Similar to the conventional nano-beam, the optical field of EPhCC is also localized between two curved graded mirror segments. Which suggests the nature of optical confinement in EPhCC is similar to conventional nano-beam. The optical field in the EPhCC is also gradually decayed from the center of the nano-beam to two ends of curved graded mirrors as light guided within the ring-shaped structure. Moreover, the optical field in EPhCC is slightly shifted away from the center of the nano-beam to the outer rim of the ring due to the high curvature. This could potentially reduce the quality factor due to mode asymmetry and leads to the design of shifted-holes EPhCC for compensation.

6.3.2 Coupling waveguide designs for evanescent coupling to EPhCC

For EPhCC structures, coupling waveguide designs are important for achieving high extinction ratio (ER) and loaded quality factor in the transmission of the micro-cavities. In this sub-section, simulations of ERs and quality factors for different coupling waveguide designs are presented. The simulation results were used as a guideline for design parameters that employed in device fabrications. They also provide insight on how the presence of coupling waveguides could affect the optical characteristics of EPhCC.

Fig. 6.4(a) shows the calculated extinction ratio and calculated loaded quality factor of the coupled fundamental mode of evanescent coupled EPhCC with different coupling waveguide designs. The period of the graded mirror is 15. The coupling waveguide widths are from 700nm to 350nm. The gap separation between the coupling waveguide and the nano-beam is fixed at 100nm. When the coupling waveguide width is decreased from 500nm to 400nm, the ER increases from ~0.3dB to ~4dB, and the loaded quality factor decreases from ~5,000 to ~1,000. This reduction of loaded quality factor is due to the increase of coupling strength from the cavity to the coupling waveguide, thus increases the total loss of the cavity and reduces its quality factor. For coupling waveguide width of >500nm, the calculated loaded quality factors also suggested the introduction of coupling waveguide into the structure significantly reduce the loaded quality factors of EPhCC. As the highest loaded quality factors of ~5,000 at 500nm coupling waveguide width is three orders lower than the intrinsic quality factor of 1.36×10^6. In addition, when the coupling waveguide width increased from 500nm to 700nm, even the coupling coefficient from the waveguide to the cavity decrease, the loaded quality factor further reduced from ~5,000 to ~2,000. This suggests the increase of

coupling waveguide width would further increase the radiation loss of the cavity. We suspect the significant reduction is related to the mode distribution of EPhCC, as shown in inset of Fig. 6.3(b), the optical field of EPhCC shifted to the outer rim of the ring due to the high curvature of bending. It results in a stronger modal overlap between the coupling waveguide and EPhCC. The ER results shown in Fig. 6.4(a) also suggests that a coupling waveguide width of <400nm is necessary to achieve high extinction ration of resonance dip in transmission spectrum. However, due to the narrow gap separation of 100nm in the simulation, the presence of coupling waveguide would also increases the radiation loss of the cavity. Therefore a stronger coupling into the cavity for achieving higher ER is required.

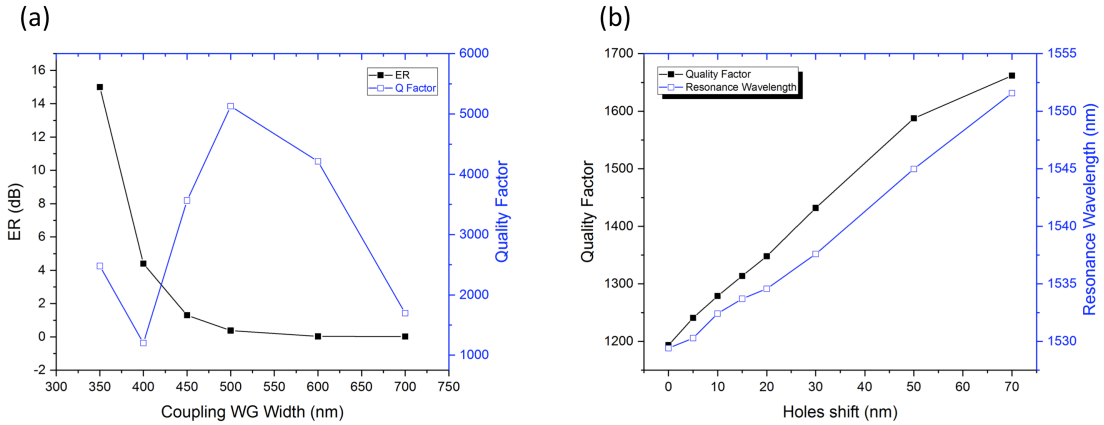

Fig. 6.4. (a) (left y axis) 3-D FDTD calculated extinction ratio and (right y axis) loaded quality factor of the coupled fundamental mode of the evanescent coupled EPhCC with different coupling waveguide designs. The gap separation between the coupling waveguide and the nano-beam is 100nm. (b) 3-D FDTD calculated (left y axis) loaded quality factor and (right y axis) resonance wavelength of the coupled fundamental mode of the evanescent coupled shifted-holes EPhCC with shifted-holes designs. The gap separation between the coupling waveguide and the nano-beam is 200nm.

In order to experimentally achieve both high ER and high loaded quality factor, the actual deigns for device fabrication consist of coupling waveguide widths as 300nm to

400nm, and separation gaps as 50nm to 500nm. There are two approaches could potentially eliminate the effect of quality factor reduction due to presence of coplanar coupling waveguides. First, we can couple the light in-to/out-of the EPhCC cavity by a coupling waveguide that positioned above (out-of-plane) or below (in-plane) the EPhCC. As the evanescent field in both out-of-plane and in-plane direction of EPhCC cavity would be weaker for TE-mode. The disadvantage of this approach is a complicated fabrication process. As precise control of thin film thickness like poly-silicon waveguide, oxide layer thickness is required. Second approach is by designing shifted-holes EPhCC that could compensate the shifting of optical mode, thus reducing its modal overlap with the coupling waveguide. The principle and simulation results of this structure will be shown in the next section.

6.3.3 Design of shifted-holes EPhCC for enhancing quality factor

In shifted-holes EPhCC, the air holes are shifted toward the outer rim of the ring-shaped EPhCC from its original positions in the original non-shifted design. By shifting the air holes toward the other rim, the effective index of inner rim regions increases and the effective index of outer rim regions decrease. It thus compensates the increased effective index of outer rim regions introduced by high-curvature in EPhCC structure. Fig. 6.4(b) shows the 3-D FDTD calculated loaded quality factor and resonance wavelength of the coupled fundamental mode of the evanescent coupled shifted-holes EPhCC with different shift-holes designs. The period of the graded mirror is 15. The coupling waveguide width is 300nm. The gap separation between the coupling waveguide and the shifted-holes EPhCC is 200nm. The shift-holes designs are 0nm (no shift), +5nm, +10nm, +15nm,

+20nm, +30nm, +50nm, +70nm, where the + sign means air holes shifted out from the center of the ring. As shown in Fig. 6.4(b), as the hole shifted from 0nm to 70nm from the center, both the quality factor and resonance wavelength are linearly increased. The quality factor has been improved from ~1,200 at 0nm shift to ~1,650 at 70nm shift, this correspond to 38% of enhancement. The resonance wavelength has been red-shifted from ~1530nm at 0nm shift to ~1552nm at 70nm bias, this correspond to a factor of 0.31. As the coupling waveguide width and gap separation remain unchanged among all designs, the red-shifted of resonance wavelengths suggests a higher portion of optical mode has been confined in the silicon when the magnitude of hole shift increase, this is well match with our intuitive explanation provided above. This resonance wavelength-tuning feature of shift-holes EPhCC designs can also be used to employ a WDM system as depicted in Fig. 6.2(b). For example, a 20nm shift-hole design would induce a resonance red-shifted of ~6.3nm.

6.4 Experimental results and discussion

Fig. 6.5(a) shows the top-view scanning electron microscope (SEM) image of the fabricated conventional butt coupled nano-beam. The structure is fabricated on a SOI platform with a 220nm thick device layer. The silicon layer is etched through to the buried oxide (BOX) layer. The details of fabrication process can be found in chapter 2. For the device shown in the SEM image, the period of the graded mirror is 12. Similar to the simulation, the design parameters used for conventional butt coupled nano-beam are: **w**=700nm, **a**=330nm, and filing factor from 0.2 to 0.1. The designs of graded mirror period are 12, 15, 20, 25 and 30. Multiple biasing conditions have been applied to structure parameters like air-holes radius and waveguide width **w** to compensate the effect of fabrication imperfection such as over-dosing during the EBL process and non-ideal anisotropic etching in the RIE process.

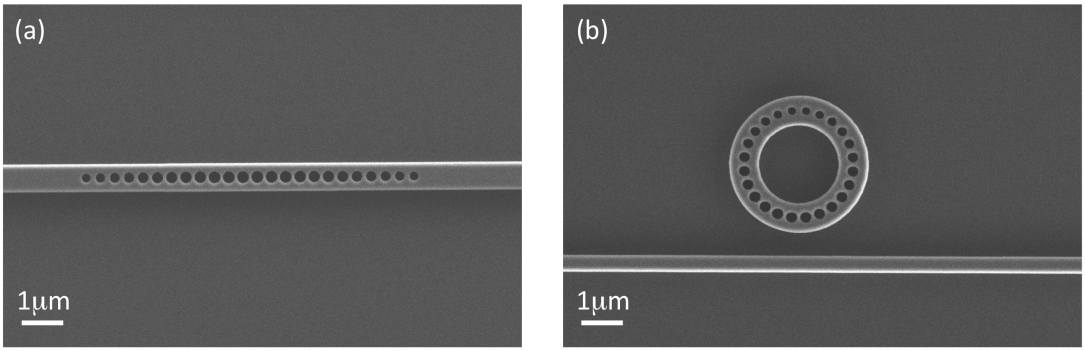

Fig. 6.5. (a) Top-view SEM image of the fabricated conventional waveguide butt coupled nano-beam. (b) Top-view SEM image of the fabricated EPhCC with a coupling waveguide. The period of the graded mirrors are 12 for both devices shown.

Fig. 6.5(b) shows the top-view SEM image of the fabricated EPhCC structure. For the device shown in the SEM image, the period of the graded mirror is 12. Similar to

conventional nano-beam, the design parameters used for EPhCC: **w**=700nm, **a**=330nm, and filing factor from 0.2 to 0.1. For coupling waveguide designs, the selected waveguide widths are 300nm, 350nm and 400nm. The gap separations are 50nm, 70nm, 90nm, 120nm, 150nm, 200nm, 300nm and 500nm. These design parameters for coupling waveguide widths and separation gaps are aimed to extract the highest measurable loaded quality factor from EPhCC by covering a wide range of loss/coupling conditions. Similar to conventional nano-beam design, multiple biasing conditions have been applied to structure parameters like air-holes radius and cavity waveguide width **w** to compensate the effect of fabrication imperfection.

6.4.1 Conventional waveguide butt coupled nano-beam

Fig. 6.6(a) shows the measured TE-polarized transmission spectra of the conventional waveguide butt coupled nano-beam with different graded mirror period. As the number of graded mirror period increases, the free spectral ranges (FSR) between fundamental mode and higher order modes reduce. The Fabry-Perot (F-P) responses at longer wavelength of >1580nm are due to the strong back reflection of the non-optimized grating couplers. The FSR between these F-P peaks are ~0.6nm. With 500mm grating-to-grating distance and group index of ~4 for silicon waveguide (and taper), the calculated FSR of ~0.62nm at 1.58mm matches well with the measured F-P FSR. For the fundamental modes, the measured (quality factor; resonance wavelength) of graded mirror period of 12, 15, 20, 25 are (2,485;1557.95nm), (9,370;1557.2nm), (27,591;1553.96nm) and (48,552;1551.74nm). The resonance peak of the fundamental mode could not be identified for graded mirror period of 30 due to weak coupling

between the cavity and the butt coupled waveguide. The loaded quality factors of graded period of 20 and 25 are 2 order of magnitude lower than the calculated quality factors by FDTD method, it is mainly due to the fabrication imperfection and the addition of BOX layer as under cladding. The measured loaded quality factors from the conventional butt coupled nano-beam in this sub-section will be used as a reference to compare the quality factors in (shifted-holes) EPhCC.

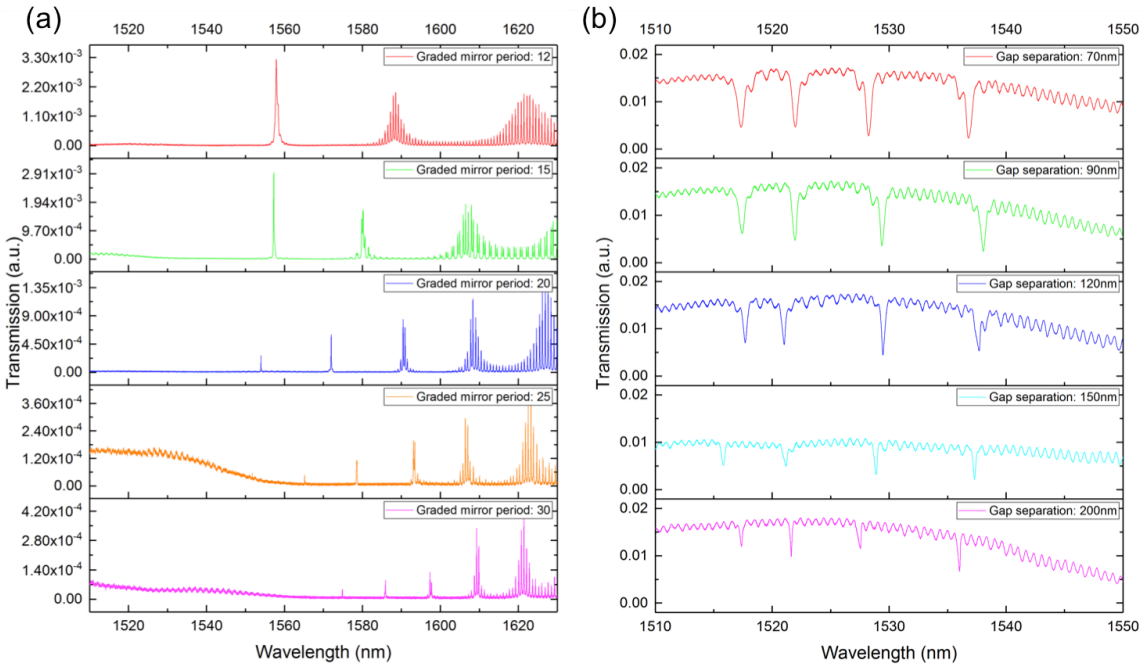

Fig. 6.6 (a). Measured TE-polarized transmission spectra of the conventional waveguide butt coupled nano-beam with different graded mirror period from 12 to 30. (b) Measured TE-polarized transmission spectra of four cascaded shifted-holes EPhCC with different gap separations from 70nm to 200nm. The period of the graded mirror is 15. The coupling waveguide width is 400nm. The shift-holes designs are 0nm, +20nm, +40nm and +60nm.

6.4.2 EPhCC and shifted-holes EPhCC

Fig. 6.6(b) shows the measured TE-polarized transmission spectra of four cascaded shifted-holes EPhCC with different gap separations from 70nm to 200nm. The period of the graded mirror is 15. The cascaded system is similar to the schematic depicted in Fig. 6.2(b), and the spacing between two EPhCC is ~3μm. The coupling waveguide width is 400nm. The shift-holes designs are 0nm, +20nm, +40nm and +60nm. Form the transmission spectra, four distant resonance dips are observed. These four resonances are from the fundamental modes of four shifted-holes EPhCC with different shifted-holes designs. In the case of 90nm gap separation, the four resonance wavelengths are 1517.2nm, 1522.5nm, 1528.7nm and 1536.9nm. These correspond to resonance wavelength shifts of 5.3nm, 6.2nm and 8.2nm, compared to the calculated resonance wavelength shift of ~6.3nm by 20nm hole shift. The difference between calculated and measured resonance wavelength shifts are mainly due to fabrication imperfection from controlling air-holes dimensions. From Fig. 6(b), the full-width-half-maximum of the resonance dips decrease as the gap separation increases, indicate a higher loaded quality factor from the EPhCC cavities. As the total loss due to out-coupling and radiation of coupling waveguide reduces.

The loaded quality factors of fundamental modes of shifted-holes EPhCCs for graded mirror period of 15 and 20 are summarized in Fig. 6.7 at different coupling conditions. Fig. 6.7(a) shows the summary of loaded quality factors of fundamental modes of shifted-holes EPhCCs for graded mirror period of 15. The loaded quality factors show a systematically enhancement with increasing amount of air holes shift. The highest loaded quality factors for 0nm, +20nm, +40nm and +60nm shift are 7,262, 12,493, 10,972 and

17,750. The loaded quality factors of the +60nm shifted-holes EPhCC provide ~2.4 fold enhancement over the no shift design. For graded period of 15, the resonance wavelengths of each shifted-holes design are controlled to a range +/- 3nm. This variation is a result of the combination of fabrication imperfection and changing of coupling waveguide position/width. As the positions/width of coupling waveguide would change the effective index of the resonance mode thus drift its resonance wavelength. In comparison to the measured loaded quality factor of 9,370 from the conventional nano-beam, the +60nm shifted-holes EPhCC provides ~89% of enhancement in loaded quality factor.

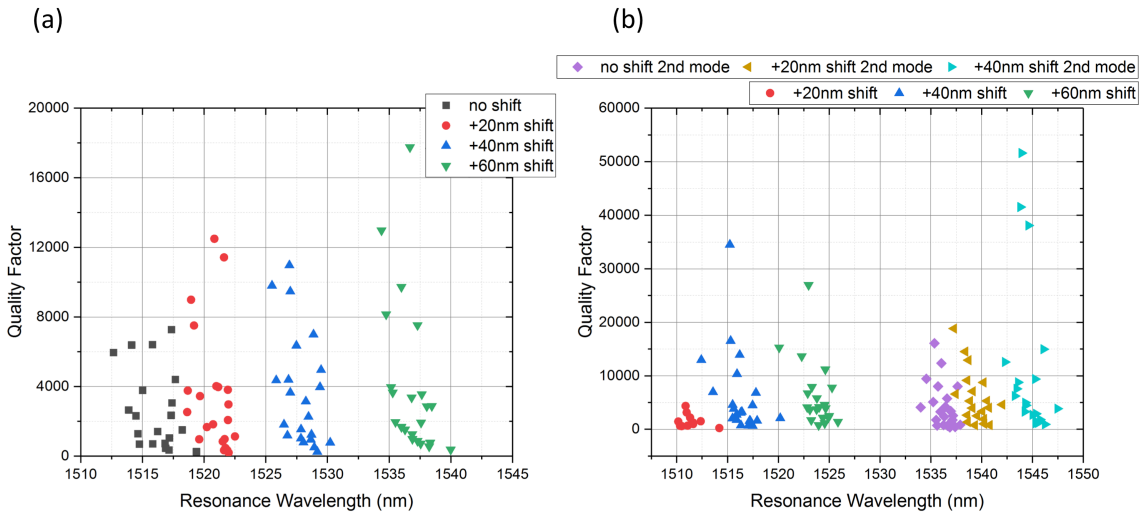

Fig. 6.7. (a) Summary of measured loaded quality factors of fundamental modes of cascaded shifted-holes EPhCCs for graded mirror period of 15. (b) Summary of measured loaded quality factors of fundamental modes (red, blue and green) and second modes (purple, orange and light blue) of cascaded shifted-holes EPhCCs for graded mirror period of 20.

Fig. 6.7(b) shows the summary of loaded quality factors of fundamental modes and second order modes of shifted-holes EPhCCs for graded mirror period of 20. Due to the fabrication variant and the longer graded mirror period, the resonance wavelengths of no

shifted-holes design and part of +20nm design are below our measurement range of 1510nm to 1630nm. As the curvature of the EPhCC has been significantly reduced with longer graded mirror period, the resonances from second order modes could be coupled by the coupling waveguide and observed in the transmission spectra. Similar to EPhCCs with graded mirror period of 15, the loaded quality factors show a systematically enhancement by increasing the shift of air holes in both fundamental modes and second order modes. The highest fundamental mode loaded quality factors for +40nm and +60nm shift are 34,515 and 26,964. For second order modes, the highest loaded quality factors for 0nm, +20nm and +40nm shift are 16,073, 18,834 and 51,619. Note that the highest measured loaded quality factor of second order mode in +40nm shift EPhCC is higher than its highest measured loaded quality factor of the fundamental mode (51,619 vs. 34,515). This also suggests that the coupling waveguide is the major source of radiation loss to the cavity, as the second order mode's modal overlap with the coupling waveguide is smaller than the fundamental mode. In comparison to the measured loaded quality factor of 27,591 from the conventional nano-beam, the second order mode of +40nm shifted-holes EPhCC provides ~87% of enhancement in quality factor. While the fundamental mode of +40nm shifted-holes EPhCC only provides ~25% of moderate enhancement.

6.5 Conclusions

In this chapter, a novel photonic device – embedded one-dimensional photonic crystal cavity has been proposed and experimentally demonstrated. The EPhCC is similar to and function as a small mode volume one-dimensional photonic crystal resonator, but with superior quality factors and easy to be implemented in a wavelength-division multiplexing system. We experimentally demonstrated a loaded quality factor of ~52,000 by a shifted-holes design on evanescently coupled EPhCC structure. This provides ~2-fold enhancement over the conventional straight-shaped nano-beam structure with identical design parameters. The measured quality factors are limited by fabrication imperfections and coupling schemes as theoretically intrinsic quality factor of EPhCC is ~10^6. The cascaded four EPhCCs system also shows feasibility to implement EPhCC in WDM system. By combing the advantages of small footprint, high quality factor and excellent resonance wavelength control, the EPhCC structure would open the door for number of applications in optical-interconnects such as small-footprint multi-wavelengths low-energy optical modulation.

7. Conclusion

In this final chapter, the summaries of different projects presented in this thesis are provided. Couples of suggestions on the future work that can be followed up from the research projects in the thesis are also suggested.

7.1 Summary

In this thesis, the design, fabrication and characterization of silicon photonics based ring-shaped photonic crystal structures have been presented. These devices combine microring structures with PhC waveguides and PhC nano-cavities, for providing enhanced optical characteristics. The photonic crystal microring resonator demonstrated as a highly sensitive bio-sensor, with more than 2-fold enhancement over traditional structures in silicon. The photonic crystal microring resonator also opens the door of new functionality on Bloch-mode selections, which could be useful for on-chip optical interconnects such as on-chip optical routings/multiplexing/de-multiplexing. Finally, a novel embedded photonic crystal cavity has been proposed and demonstrated with superior quality factor over conventional structure. This structure is fully compatible into a small footprint WDM system. It thus can be used to construct a compact on-chip multi-channel lasers/modulator. The research results reported in this thesis show that by employing extensive device engineering, creating novel nano-photonic devices and understanding their optical characteristics, we could advance the applications of photonic structures by controlling light in a space of nanometer dimensions. Therefore these techniques and know-how of photonic designs on nano-photonic structures would eventually solve the

existing problems to benefit the fields of medical diagnostics, interconnects and optical communications.

7.2 Future work

7.2.1 Enhancing the light-matter interaction in PhCR for biosensing

In chapter 3 we presented the applications of PhCR structures in biosensing. The results indicate that a non-optimized PhCR structure could already provide more than 2-fold enhancement in bulk index sensing and surface sensing of DNA and protein bio-molecules. However, there are still several ways to further enhance the sensing performance of PhCR structures.

First, the sensing experiment can be done when the PhCR is operated in the air-band mode like in [71]. In the demonstrated results in this thesis, the light was still confined majorly in the silicon region of the PhCR structure as the resonances modes were still sitting in the silicon band. By modifying the waveguide width and size of air holes (filling factors), we could also design a PhCR with resonance wavelengths of air-band modes close to 1510nm to 1630nm. Although this approach also increase the difficulties of achieving the mode matching between lower-effective index PhC waveguide and silicon waveguide, it could be solved by using our reported chirped PhC taper in chapter 5. As a result, the air-band mode PhCR sensor could retains all the advantages of the PhCR provide as a bio-sensor, but with a even higher sensitivity.

Second, we can combine the advantages of slot-waveguide into the PhCR. As slot waveguide structures can confine light into the lower index region by utilizing the properties of electric field discontinuity [112]. Therefore the resulted slot PhCR could be

in principle working in a silicon band of dispersive curve, but confine most of its light in the air regions that could be accessible by bio-molecules to increase its sensing performance. Note that this new slot PhCR design may altered the resonance wavelength quite a bit so extensive simulation and modeling work have to be done before fabrication and experimental demonstration.

Third, we can also make the PhCR sensor in a suspended platform so all the surface around the structure will be exposed to air. In the current demonstration the PhCR was attached to the BOX layer so the bottom layer of the structure could not be able to interact with the functionalized bio-molecules. This not only decreases the sensing performance of the exist structure, but also lowering the quality factor as PhC devices are sensitive to asymmetric configuration, which would induce extra radiation losses. Therefore, a simple process of buffered oxide etching (BOE) process could provide better results in both quality factor and sensitivity.

7.2.2 PhCR based add-drop filter arrays for on-chip optical routing

In chapter 4, we presented the results of Bloch-modes selection by employing the highly dispersive PhCR structure. By utilizing the macroscopic beating mode patterns of PhCRs, different sub-set of optical modes can be taped out by output coupling waveguides (drop ports) at different azimuthal angles. This feature and phenomenon can be useful for on-chip interconnects such as optical routing and add-drop filters, in where the requirement of optical devices footprint would be tight.

In order to expand the device into a system level building block, we can cascade the PhCRs as an add-drop filter arrays like prior demonstrated results by silicon microring [113]. Unlike silicon micoring, in the new system of multi-channels PhCR arrays, each PhCR can pass/through multiple channels if we design the output coupling waveguides positioned as 90 degrees and 180 degrees respect to the input waveguide. Therefore it could be significantly reduce the footprint of such a multi-channel arrays routing network. System level analysis by transfer matrix and block diagrams will be required to design the actual system architecture of there arrays.

7.2.3 Embedded nano-beam PhC cavity based optical modulators

In chapter 6, we proposed, designed and demonstrated a novel embedded photonic crystal cavity (EPhCC) structure that has superior quality factor and WDM compatibility over conventional nano-beam devices. The results in chapter 6 are aimed to provide a systematic study on the optical properties like mode volumes, mode profiles and quality factors on the EPhCC devices. However, the EPhCC devices could also be useful for many of applications due to its high-Q, low mode volume and compact size.

One of the major applications that EPhCC can become beneficial is high-speed optical modulation. Due to its high quality factor, small mode volume and high extinction ratio by controlling its coupling condition, EPhCC could be designed as a compact, high-speed, low-energy optical modulator. Moreover, since the structure is coupled evanescently to the feeding waveguide, it can be cascaded and formed a compact WDM system. Therefore it can be combined as a modulators array for multi-channels optical modulator too.

There are couples of different active structures configuration can lead to the optical modulation by the free carrier plasma dispersion effect in silicon [10]. Such as forward biasing the p-i-n diode for carrier injection [114], reverse biasing a p-n diode [115] and carrier accumulation of a capacitor [116]. Among them, the carrier accumulation of capacitor would be most suitable for making a modulator although it is difficult to be fabricated. It provides the best balance between optical losses, energy consumption and modulation speed.

BIBLIOGRAPHY

1. L. Pavesi, “Will silicon be the photonic material of the third millennium?” J. Phys. Condens. Matter, 15, R1169-R1196, 2003

2. Z. Zhang et al., "Hybrid photonic integration on a polymer platform", *J. Photon.*, vol. 2, no. 3, pp. 1005-1026, 2015

3. R. Nagarajan et al., “InP photonic integrated circuits”, IEEE Journal of Selected Topics in Quantum Electronics, Vol. 16, No.5, 2010

4. L. Pavesi and D. J. Lockwood, Silicon Photonics, Springer, 2004

5. G. T. Reed, Silicon Photonics the state of the art, Wiley, 2009

6. D. A. B. Miller, “Rationale and challenges for optical interconnects to electronic chips”, Proceedings of IEEE, 99, 728, 2000

7. S. E. Miller, “Integrated optics: an Introduction”, Bell Sys. Tech. J., Vol. 48, 2059-2069, 1969

8. R. A. Soref and J. P. Lorenzo, “Single-crystal silicon – a new material for 1.3 and 1.6 μm integrated-optical components”, Electronics Letters, 21, 953-954, 1985

9. R. A. Soref and J. P. Lorenzo, “All-silicon active and passive guided-wave components for $\lambda = 1.3$ μm and 1.6 μm”, IEEE Journal of Quantum Electronics, QE-22, 873-879, 1986

10. R. A. Soref and B. R. Bennett, “Electrooptical Effect in Silicon,” IEEE Journal of Quantum Electronics Vol. QE-23, 123-129, 1987

11. R. A. Soref, “Silicon- based optoelectronics”, Proceedings of the IEEE, Vol. 81, 1687-1706, 1993

12. R. A. Soref, “The past, present and future of silicon photonics”, IEEE Journal of Selected Topics in Quantum Electronics, Vol. 12, 1678-1687, 2006

13. A. W. Fang et al., “Electrically pumped hybrid AlGaInAs-silicon evanescent laser”, Optics Express, Vol. 14, No. 20, 9203-9210, 2006

14. J. Michel et al., “High-performance Ge-on-Si photodetectors”, Nature photonics, Vol.4, 527-534, 2010

15. L. Liao et al., “40 Gbit/s silicon optical modulator for high-speed applications”, Electronics Letters, Vol. 43, No. 22, 2007

16. C. Gunn, “CMOS photonics for high-speed interconnects”, IEEE Micro, Vol. 26, 58-66, 2006

17. European 450mm Equipment & Materials Initiative; http://www.eemi450.org/

18. J. D. Joannopoulos, S. G. Johnson, J. N. Winn & R. D. Meade, Photonic Crystals: Molding the Flow of Light, Princeton Univ. Press, 2011

19. E. Yablonovitch, "Inhibited Spontaneous Emmission in Solid-State Physics and Electronics," Phys. Rev. Lett., 58, 2059, 1987

20. S John, "Strong localization of photons in certain disordered dielectric superlattices", Phys. Rev. Lett., 58, 2486, 1987

21. E. Yablonovitch, T. J. Gmitter and K. M. Leung, "Photonic Band Structure: The Face-Centered-Cubic Case Employing Nonspherical Atoms", Phys. Rev. Lett.,67, 2295, 1991

22. T. F. Krauss, R. M. De La Rue and S. Brand, "Two-dimensional photonic-bandgap structures operating at near-infrared wavelengths", Nature, 383, 699, 1996

23. S. J. McNab, N. Moll and Y. A. Vlasov, "Ultra-low loss photonic integrated circuit with membrane-type photonic crystal waveguides", Optics Express, 11, 2927, 2003

24. P. Ma, P. Kaspar, Y. Fedoryshyn, P. Strasser, and H. Jäckel, "InP-based planar photonic crystal waveguide in honeycomb lattice geometry for TM-polarized light," Optics Letters, 34, 1558, 2009

25. B. Ellis, M. Mayer et al., "Ultralow-threshold electrically pumped quantum-dot photonic-crystal nanocavity laser", Nature Photonics, 5. 291, 2011

26. T. Baba, "Slow light in photonic crystal", Nature Photonics, 2, 465, 2008

27. B. Corcoran, C. Monat et al, "Green light emission in silicon through slow-light enhanced third-harmonic generation in photonic crystal waveguides", Nature Photonics, 3, 206, 2009

28. B. Corcoran, C. Monat et al, "Optical signal processing on a silicon chip at 640Gb/s using slow-light", Optics Express, 18, 7770, 2010

29. J. Li, T. White, L. O'Faolain, A. Gomez-Iglesias, and T. Krauss, "Systematic design of flat band slow light in photonic crystal waveguides," Opt Express 16, 6227–6232, 2008

30. Y. Akahane, T. Asano, B. Song, and S. Noda, "High-Q photonic nanocavity in a two-dimensional photonic crystal," Nature 425, 944–947, 2003

31. J. Gao, J. F. Mcmillan, M.-C. Wu, J. Zheng, S. Assefa, and C. W. Wong, "Demonstration of an air-slot mode-gap confined photonic crystal slab nanocavity with ultrasmall mode volumes," Appl Phys Lett 96, 051123, 2010

32. M. Lee and P. Fauchet, "Two-dimensional silicon photonic crystal based biosensing platform for protein detection," Opt. Express, Vol. 15, 4530-4535, 2007

33. Y. Jiang, W. Jiang, L. Gu, X. Chen & R. T. Chen, "80-micron interaction length silicon photonic crystal waveguide modulator," Appl. Phys. Lett., **87**, 221105, 2005

34. K. Yee, "Numerical solution of initial boundary value problems involving Maxwell's equations in isotropic media," Antennas and Propagation **14**, 302– 307, 1966

35. The Yee cell, https://fdtd.wikispaces.com/The+Yee+Cell

36. Lumerical Solutions Inc., FDTD Solutions (www.lumerical.com)

37. S. G. Johnson and J. D. Joannopoulos, "Block-iterative frequency-domain methods for Maxwell's equations in a planewave basis," Opt Express **8**, 173– 190, 2001

38. MIT Photonic Bands, http://ab-initio.mit.edu/wiki/index.php/MIT_Photonic_Bands

39. CNMS, ORNL https://www.ornl.gov/facility/cnms

40. IEN, GATECH http://cleanroom.ien.gatech.edu

41. SOITEC, https://www.soitec.com/en

42. X. Xu, H. Subbaraman, J. Covey, D. Kwong, A. Hosseini, and R. Chen, "Complementary metal–oxide–semiconductor compatible high efficiency subwavelength grating couplers for silicon integrated photonics," Appl. Phys. Lett. **101**, 031109, 2012

43. M. Iqbal, M. Gleeson, B. Spaugh, F. Tybor, W. Gunn, M. Hochberg, T. Baehr-Jones, R. Bailey, and L. Gunn, "Label-Free biosensor arrays based on silicon ring resonators and high-speed optical scanning instrumentation," IEEE J. Sel. Top. Quantum Electron. **16**, 654–661, 2010

44. D. Xu, M. Vachon, A. Densmore, R. Ma, A. Delâge, S. Janz, J. Lapointe, Y. Li, G. Lopinski, and D. Zhang, "Label-free biosensor array based on silicon-on-insulator ring resonators addressed using a WDM approach," Opt. Lett. **35**, 2771-2773, 2010

45. A. Qavi, J. Kindt, M. Gleeson and R. Bailey, "Anti-DNA:RNA antibodies and silicon photonic microring resonators: increased sensitivity for multiplexed microRNA detection," Anal. Chem. **83**, 5949-5956, 2011

46. K. De Vos, I. Bartolozzi, E. Schacht, P. Bienstman, and R. Baets, "Silicon-on-Insulator microring resonator for sensitive and label-free biosensing," Opt. Express **15**, 7610-7615, 2007

47. F. Liang, N. Clarke, P. Patel, M. Loncar, and Q. Quan, “Scalable photonic crystal chips for high sensitivity protein detection,” Opt. Express **21**, 32306-32312, 2013

48. M. Lee and P. Fauchet, “Two-dimensional silicon photonic crystal based biosensing platform for protein detection,” Opt. Express **15**, 4530-4535, 2007

49. W. Lai, S. Chakravarty, Y. Zou, and R. Chen, “Silicon nano-membrane based photonic crystal microcavities for high sensitivity bio-sensing,” Opt. Lett. **37**, 1208-1210, 2012

50. C. Kang, C. Phare, Y. Vlasov, S. Assefa, and S. Weiss, “Photonic crystal slab sensor with enhanced surface area,” Opt. Express **18**, 27930-27937, 2010

51. M. Lee and P. Fauchet, “Nanoscale microcavity sensor for single particle detection,” Opt. Lett. **33**, 3284-3286, 2008

52. S. Buswell, V. Wright, J. Buriak, V. Van, and S. Evoy, “Specific detection of proteins using photonic crystal waveguides,” Opt. Express **16**, 15949-15957, 2008

53. R. Lequin, “Enzyme immunoassay (EIA)/enzyme-linked immunosorbent assay (ELISA),” Clin. Chem. **51**, 2415-2418, 2005

54. T. Claes, J. Molera, K. De Vos, E. Schacht, R. Baets, and P. Bienstman, “Label-free biosensing with a slot-waveguide-based ring resonator in silicon on insulator,” IEEE Photon. J. **1**, 197–204, 2009

55. S. Hu, K. Qin, I. Kravchenko, S. Retterer, and S. Weiss, “Suspended micro-ring resonator for enhanced biomolecule detection sensitivity,” Proc. of SPIE **8933**, 893306, 2014

56. J. Flueckiger, S. Schmidt, V. Donzella, A. Sherwali, D. Ratner, L. Chrostowski, and K. Cheung, “Sub-wavelength grating for enhanced ring resonator biosensor,” Opt. Express **24**, 15672-15686, 2016

57. C. Kang, S. Weiss, Y. Vlasov, and S. Assefa, “Optimized light–matter interaction and defect hole placement in photonic crystal cavity sensors,” Opt. Lett. **37**, 2850-2852, 2012

58. M. Scullion, A. Di Falco, and T. Krauss, “Slotted photonic crystal cavities with integrated microfluidics for biosensing applications,” Biosens. Bioelectron. **27**, 101-105, 2011

59. S. Chakravarty, Y. Zou, W. Lai and R. Chen, “Slow light engineering for high Q high sensitivity photonic crystal microcavity biosensors in silicon,” Biosens. Bioelectron. **38**, 170-176, 2012

60. J. Lee and P. Fauchet, “Slow-light dispersion in periodically patterned silicon microring resonators,” Opt. Lett. **37**, 58-60, 2012

61. D. Goldring, U. Levy, and D. Mendlovic, "Highly dispersive micro-ring resonator based on one dimensional photonic crystal waveguide design and analysis," Opt. Express **15**, 3156-3168, 2007

62. K. McGarvey-Lechable and P. Bianucci, "Maximizing slow-light enhancement in one-dimensional photonic crystal ring resonators," Opt. Express **22**, 26032-26041, 2014

63. K. McGarvey-Lechable, T. Hamidfar, D. Patel, L. Xu, D. V. Plant, and P. Bianucci, "Slow light in mass-produced, dispersion-engineered photonic crystal ring resonators," Opt. Express **25**, 3916-3926, 2017

64. W. Bogaerts, R. Baets, P. Dumon, V. Wiaux, S. Beckx, D. Taillaert, B. Luyssaert, J. Van Campenhout, P. Bienstman, D. Van Thourhout, "Nanophotonic waveguides in silicon-on-insulator fabricated with CMOS technology," J. Lightw. Technol. **23**, 401-412, 2005

65. S. Pal, E. Guillermain, R. Sriram, B. Miller and P. Fauchet, "Silicon photonic crystal nanocavity-coupled waveguides for error-corrected optical biosensing," Biosens. Bioelectron. **26**, 4024-4031, 2011

66. S. Lo, S. Hu, S. Weiss, and P. Fauchet, "Photonic crystal microring resonator based sensors," in *Conference on Lasers and Electro-Optics: 2014*, OSA Technical Digest (online) (Optical Society of America, 2014), paper JTu4A.79.

67. D. Urbonas, A. Balčytis, K. Vaškevičius, M. Gabalis, and R. Petruškevičius, "Air and dielectric bands photonic crystal microringresonator for refractive index sensing," Opt. Lett. **41**, 3655-3658, 2016

68. F. De Leonardis, C. Campanella, B. Troia, A. Perri, and V. Passaro, "Performance of SOI Bragg grating ring resonator for nonlinear sensing applications," Sensors **14**, 16017–16034, 2014

69. C. Campanella, F. Leonardis, L. Mastronardi, P. Malara, G. Gagliardi, and V. Passaro, "Investigation of refractive index sensing based on Fano resonance in fiber Bragg grating ring resonators," Opt. Express **23**, 14301-14313, 2015

70. S. Hu, Y. Zhao, K. Qin, S. Retterer, I. Kravchenko, and S. Weiss, "Enhancing the sensitivity of label-free silicon photonic biosensors through increased probe molecule density," ACS Photon. **1**, 590-597, 2014

71. G. Gao, Y. Zhang, H. Zhang, Y. Wang, Q. Huang and J. Xia, "Air-mode photonic crystal ring resonator on silicon-on-insulator," Sci. Rep. **6**, 19999, 2016

72. W. Bogaerts, P. De Heyn, T. Van Vaerenbergh, K. DeVos, S. K. Selvaraja, T. Claes, P. Dumon, P. Bienstman, D. Van Thourhout, R. Baets, "Silicon microring resonators," Laser Photon. Rev. 6, 47–73, 2012

73. B. Little, S. Chu, H. Haus, J. Foresi, and J.-P. Laine, “Microring resonator channel dropping filters,” J. Lightwave Technol. 15, 998–1005, 1997

74. S. Xiao, M. Khan, H. Shen, and M. Qi, "A highly compact third-order silicon microring add-drop filter with a very large free spectral range, a flat passband and a low delay dispersion," Opt. Express 15, 14765-14771, 2007

75. Q. Xu, B. Schmidt, S. Pradhan, and M. Lipson, “Micrometre-scale silicon electro-optic modulator,” Nature. 435, 325-327, 2005

76. P. Dong, W. Qian, H. Liang, R. Shafiiha, D. Feng, G. Li, J. Cunningham, A. Krishnamoorthy, and M. Asghari, "Thermally tunable silicon racetrack resonators with ultralow tuning power," Opt. Express 18, 20298-20304, 2010

77. F. Xia, L. Sekaric, and Y. Vlasov, “Ultra-compact optical buffers on a silicon chip,” Nature Photonics 1, 65-71, 2007

78. Q. Xu and M. Lipson, "All-optical logic based on silicon micro-ring resonators," Opt. Express 15, 924-929, 2007

79. C. Li, L. Zhou, and A. Poon, "Silicon microring carrier-injection-based modulators/switches with tunable extinction ratios and OR-logic switching by using waveguide cross-coupling," Opt. Express 15, 5069-5076, 2007

80. R. Ji, L. Yang, L. Zhang, Y. Tian, J. Ding, H. Chen, Y. Lu, P. Zhou, and W. Zhu, "Five-port optical router for photonic networks-on-chip," Opt. Express 19, 20258-20268, 2011

81. D. Goldring, U. Levy, and D. Mendlovic, "Highly dispersive micro-ring resonator based on one dimensional photonic crystal waveguide design and analysis," Opt. Express 15, 3156-3168, 2007

82. S. Lo, S. Hu, G. Gaur, Y. Kostoulas, S. Weiss, and P. Fauchet, "Photonic crystal microring resonator for label-free biosensing," Opt. Express 25, 7046-7054, 2017

83. M. Loncar, D. Nedelikovic, T. Pearsall, J. Vuckovic, A. Scherer, S. Kuchinsky, and D. Allan, “Experimental and theoretical confirmation of Bloch-mode light propagation in planar photonic crystal waveguides,”Appl. Phys. Lett. 80, 1689, 2002

84. S. Ha, A. Sukhorukov, K. Dossou, L. Botten, C. de Sterke, and Y. Kivshar, “Bloch-mode extraction from near-field data in periodic waveguides,”Opt. Lett. 34, 3776, 2009

85. K. Tsia and A. Poon, “Dispersion-guided resonances in two-dimensional photonic-crystal-embedded microcavities,” Opt. Express 12, 5711, 2004

86. I. Giuntoni, A. Gajda, M. Krause, R. Steingrüber, J. Bruns, and K. Petermann, "Tunable Bragg reflectors on silicon-on-insulator rib waveguides," Opt. Express **17**, 18518-18524, 2009

87. K. Ikeda, M. Nezhad, and Y. Fainman, "Wavelength selective coupler with vertical gratings on silicon chip,"Appl. Phys. Lett. **92**, 201111, 2008

88. P. Cheben, P. J. Bock, J. H. Schmid, J. Lapointe, S. Janz, D. Xu, A. Densmore, A. Delâge, B. Lamontagne, and T. Hall, "Refractive index engineering with subwavelength gratings for efficient microphotonic couplers and planar waveguide multiplexers," Opt. Lett. **35**, 2526-2528, 2010

89. M. Fujita and T. Baba, "Microgear laser," Appl. Phys. Lett. **80**, 2051, 2002

90. L. Mahler, A. Tredicucci, F. Beltram, C. Walther, J. Faist, B. Witzigmann, H. E. Beere, and D. A. Ritchie, "Vertically emitting microdisk lasers," Nat. Photonics 3, 46, 2009

91. K. Yamada, "Silicon photonic wire waveguides: fundamental and applications," in Silicon Photonics II, Vol. 119

92. D. S. Weiss, V. Sandoghdar, J. Hare, V. Lefèvre-Seguin, J.-M. Raimond, and S. Haroche, "Splitting of high-Q Mie modes induced by light backscattering in silica microspheres," Opt. Lett. **20**, 1835-1837, 1995

93. T. Yamamoto, M. Notomi, H. Taniyama, E. Kuramochi, Y. Yoshikawa, Y. Torii, and T. Kuga, "Design of a high-Q air-slot cavity based on a width-modulated line-defect in a photonic crystal slab," Opt Express **16**, 13809–13817, 2008

94. K. Vahala, *Optical Microcavities* (World Scientific Publishing, 2004).

95. D. Mori, S. Kubo, H. Sasaki, and T. Baba, "Experimental demonstration of wideband dispersion-compensated slow light by a chirped photonic crystal directional coupler," Opt Express **15**, 5264–5270 (2007).

96. T. Tanabe, M. Notomi, E. Kuramochi, A. Shinya, and H. Taniyama, "Trapping and delaying photons for one nanosecond in an ultrasmall high-Q photonic-crystal nanocavity," Nature Photonics **1**, 49–52, 2007

97. J. Foresi, P. Villeneuve, J. Ferrera, E. Thoen, G. Steinmeyer, S. Fan, J. Joannopoulos, L. Kimerling, H. Smith, and E. Ippen, "Photonic-bandgap microcavities in optical waveguides," Nature **390**, 143–145, 1997

98. D. Englund, D. Fattal, E. Waks, G. Solomon, B. Zhang, T. Nakaoka, Y. Arakawa, Y. Yamamoto, and J. Vuckovic, "Controlling the Spontaneous Emission Rate of Single Quantum Dots in a Two-Dimensional Photonic Crystal," Phys. Rev. Lett. **95**, 013904, 2005

99. M. Notomi, A. Shinya, S. Mitsugi, G. Kira, E. Kuramochi, and T. Tanabe, "Optical bistable switching action of Si high-Q photonic-crystal nanocavities," Opt Express **13**, 2678–2687, 2005

100. B. S. Song, S. Noda, T. Asano, and Y. Akahane, "Ultra-high-Q photonic double-heterostructure nanocavity," Nat. Mater. **4**, 207–210, 2005

101. S. Tomljenovic-Hanic, C. M. de Sterke, and M. J. Steel, "Design of high-Q cavities in photonic crystal slab heterostructures by air-holes infiltration," Opt. Express 14, 12451–12456, 2006

102. E. Kuramochi, M. Notomi, S. Mitsugi, A. Shinya, T. Tanabe, and T. Watanabe, "Ultrahigh-Q photonic crystal nanocavities realized by the local width modulation of a line defect," Appl. Phys. Lett. 88, 041112, 2006

103. K. Nozaki, S. Kita and T. Baba, "Room temperature continuous wave operation and controlled spontaneous emission in ultrasmall photonic crystal nanolaser," Opt. Express 15, 7506–7514, 2007

104. Y. Tanaka, T. Asano, and S. Noda, "Design of photonic crystal nanocavity with **Q**-factor of ~10^9," J. Lightwave Technol. 26, 1532, 2008

105. M. Notomi, E. Kuramochi, and H. Taniyama, "Ultrahigh-Q nanocavity with 1D Photonic Gap," Opt. Express, 16, 11095, 2008

106. P. Velha, E. Picard, T. Charvolin, E. Hadji, J. C. Rodier, P. Lalanne, and E. Peyrage, "Ultra-high Q/V Fabry-Perot microcavity on SOI substrate," Opt. Express 15, 16090–16096, 2007

107. S. Reitzenstein, C. Hofmann, A. Gorbunov, M Strauβ , S. H. Kwon, C. Schneider, A. Loffler, S. Hofling, M. Kamp, and A. Forchel, "AlAs/GaAs micropillar cavities with quality factors exceeding 150000," Appl. Phys. Lett. 90, 251109, 2007

108. A. R. Md Zain, N. P. Johnson, M. Sorel, and R. M. De La Rue, "Ultra high quality factor one dimensional photonic crystal/photonic wire micro-cavities in silicon-on-insulator (SOI)," Opt. Express 16, 12084, 2008

109. Y. Zhang and M. Loncar, "Ultra-high quality factor optical resonators based on semiconductor nanowires." Opt. Express 16, 17400–17409, 2008

110. Q. Quan, P. B. Deotare, and M. Loncar, "Photonic crystal nanobeam cavity strongly coupled to the feeding waveguide," Appl. Phys. Lett. 96, 203102, 2010

111. Q. Quan and M. Loncar, "Deterministic design of wavelength scale, ultra-high Q photonic crystal nanobeam cavities," Opt. Express 19, 18529-18542, 2011

112. V. R. Almeida, Q. F. Xu, C. A. Barrios, and M. Lipson. Guiding and confining light in void nanostructure. Optics Letters, 29(11):1209, 2004

113. F. Xu and A. Poon, "Silicon cross-connect filters using microring resonator coupled multimode-interference-based waveguide crossings," Opt. Express 16, 8649-8657, 2008

114. B. Schmidt, Q. Xu, J. Shakya, S. Manipatruni, and M. Lipson, "Compact electro-optic modulator on silicon-on-insulator substrates using cavities with ultra-small modal volumes," Opt. Express 15, 3140-3148, 2007

115. W. M. Green et al., "Ultra-compact, low RF power, 10 Gb/s silicon Mach-Zehnder modulator", Optics Express, Vol. 15, No.25, 17106-17113, 2007

116. A. Liu et al., "A high-speed silicon optical modulator based on a metal-oxide-semiconductor capacitor", Nature, Vol. 427, 615-618, 2004